Appendix A Site M0065

Site M0065[1]

T. Andrén, B.B. Jørgensen, C. Cotterill, S. Green, E. Andrén, J. Ash, T. Bauersachs, B. Cragg, A.-S. Fanget, A. Fehr, W. Granoszewski, J. Groeneveld, D. Hardisty, E. Herrero-Bervera, O. Hyttinen, J.B. Jensen, S. Johnson, M. Kenzler, A. Kotilainen, U. Kotthoff, I.P.G. Marshall, E. Martin, S. Obrochta, S. Passchier, N. Quintana Krupinski, N. Riedinger, C. Slomp, I. Snowball, A. Stepanova, S. Strano, A. Torti, J. Warnock, N. Xiao, and R. Zhang[2]

Chapter contents

[1] Andrén, T., Jørgensen, B.B., Cotterill, C., Green, S., Andrén, E., Ash, J., Bauersachs, T., Cragg, B., Fanget, A.-S., Fehr, A., Granoszewski, W., Groeneveld, J., Hardisty, D., Herrero-Bervera, E., Hyttinen, O., Jensen, J.B., Johnson, S., Kenzler, M., Kotilainen, A., Kotthoff, U., Marshall, I.P.G., Martin, E., Obrochta, S., Passchier, S., Quintana Krupinski, N., Riedinger, N., Slomp, C., Snowball, I., Stepanova, A., Strano, S., Torti, A., Warnock, J., Xiao, N., and Zhang, R., 2015. Site M0065. *In* Andrén, T., Jørgensen, B.B., Cotterill, C., Green, S., and the Expedition 347 Scientists, *Proc. IODP,* 347: College Station, TX (Integrated Ocean Drilling Program).
doi:10.2204/iodp.proc.347.109.2015
[2] **Expedition 347 Scientists' addresses.**

Introduction

During Integrated Ocean Drilling Program (IODP) Expedition 347, cores were recovered from three holes at Site M0065 (Bornholm Basin), with an average site recovery of 99%. The water depth was 84.3 m, with a tidal range of <10 cm. Existing data sets, including seismic reflection profiles, were evaluated prior to coring to attempt to guide the initial drilling with an anticipated lithologic breakdown. The total time spent at this station was 2.59 days.

Operations

Transit to Hole M0065A

The vessel left Hole M0064D for Site M0065 (proposed Site BSB-7) in the Bornholm Basin at 1200 h on 23 October 2013. Position was established over Hole M0065A at 1400 h on 23 October, and operations commenced with a camera survey (Table **T1**).

Hole M0065A

A remotely operated vehicle survey was carried out on a transect over the locations for Holes M0065A, M0065B, and M0065C. This was required by the risk assessment for this site because of the possibility of chemical contaminants being present at the seabed. Following the survey, coring operations commenced. The uppermost 2 m was washed down, to avoid contamination, and additional personal protective equipment (PPE) was worn for the first run. The first run was recovered at 1850 h, and coring continued smoothly, with eight cores recovered before midnight.

Coring in Hole M0065A continued on 24 October 2013. Initially, piston coring was used to recover the clay lithologies before switching to a combination of open holing and hammer sampling in order to maximize recovery in the sandier lithologies. This continued to 73.90 mbsf, when bedrock was encountered. The hole was then flushed with mud and prepared for downhole logging, with the pipe tripped back to 14 meters below seafloor (mbsf).

Logging operations started in Hole M0065A on 24 October with rigging up the Weatherford logging setup. The first tool string comprised the total gamma ray and induction tools and reached 42 mbsf, where the uplog commenced. The second tool string

doi:10.2204/iodp.proc.347.109.2015

comprising total gamma ray and spectral gamma ray tools reached only 16 mbsf. The decision was taken to run in hole with the drill pipe to 45 mbsf and do a wiper trip of the hole. After this, rig up for logging started again. The tool string with total gamma ray and spectral gamma ray was deployed again but only reached 20 mbsf. Following this attempt, downhole logging operations terminated.

A total of 28 cores and 15 open-hole sections were recovered from Hole M0065A to a maximum depth of 73.90 mbsf. Hole recovery was 99.19% when the open-hole sections were discounted.

Hole M0065B

The vessel moved under dynamic positioning to Hole M0065B, arriving on site at 2230 h on 24 October 2013, when operations commenced. To avoid potential chemical contamination at the surface, the hole was washed down to 3 m before coring commenced.

On the morning of 25 October (to 1010 h) coring operations ran smoothly, with 13 piston cores recovered and 2 hammer samples conducted in sandier material at the base of the hole. The final hammer sample recovered a smear of sand, and it was decided that no further penetration was required at this hole.

A total of 16 cores were recovered from Hole M0065B to 49.30 mbsf, with two open-hole sections. Hole recovery was 99.28% when the two open-hole sections (5 m) were removed from the calculation.

Hole M0065C

The vessel bumped over to begin coring Hole M0065C at 1110 h on 25 October 2013. Again, the hole was washed down to 2 mbsf and appropriate PPE was worn for the initial core run. Piston coring continued until 0010 h on 26 October, when the hole ended at 47.9 mbsf. The drill floor was then prepared for downhole logging operations.

Logging operations started in Hole M0065C on 26 October at 0105 h with rigging up the Weatherford logging setup after the drill pipe was tripped to 14 mbsf. The first tool string comprising total gamma ray, spectral gamma ray, and sonic tools reached ~40 mbsf, where an uplog was started. The second tool string with total gamma ray and microimager tools reached 40 mbsf, and a high-resolution uplog was performed. Logging operations were finished at 0330 h.

A total of 14 cores were recovered from Hole M0065C to 47.9 mbsf, with one open-hole section at the top of the hole. Hole recovery was 99.61% when the open hole-section was discounted.

Lithostratigraphy

At Site M0065, cores were recovered from three holes (M0065A–M0065C) at a water depth of 84 m. Hole M0065A reached a total depth of 73.9 mbsf, Hole M0065B reached 49.3 mbsf, and M0065C reached 47.9 mbsf. In Hole M0065A, core recovery was very low in the lowermost part, so core material available for onshore description only includes sediment to 46.6 mbsf.

Site M0065 is located in the vicinity of a World War II ammunition dump, and special precautions were required. In Hole M0065A, the uppermost 2 mbsf was washed down to avoid contamination and additional PPE was worn for the first run (see **"Operations"**). Gas expansion characterized the upper few meters, whereas the lower part was in general only slightly disturbed by coring.

Piston coring was carried out down to a hard sand layer at 46 mbsf before switching to a combination of open holing and hammer sampling to maximize recovery in the sandier lithologies (see **"Operations"**). This continued to 73.90 mbsf, where bedrock was encountered. Holes M0065B and M0065C followed the same procedure but were stopped as they entered the hard sand layer. Hole M0065C was dedicated to microbiological sampling.

Lithostratigraphic divisions are based on descriptions on the cut face of the split core from Holes M0065A and M0065B, which gives the most complete composite record of Holocene and late glacial sediments, with a core recovery of ~95% for the uppermost 40 m. Supplementary information is collected from Hole M0065C in addition to smear slide studies.

Site M0065 is divided into three lithostratigraphic units (Units I–III; Figs. **F1**, **F2**). Unit I (0–9 mbsf) is composed of organic-rich clays containing fragments of bivalve shells and organic remnants. Unit II (9–13 mbsf) is gray clay dominated by iron sulfide lamination in the upper part; freshwater diatoms were found in a smear slide. The lowermost Unit III is divided in three clay subunits: Subunit IIIa (13–36 mbsf) is grayish brown contorted clay, Subunit IIIb (36–36.6 mbsf) is dark gray homogeneous clay, and Subunit IIIc (36.6–49 mbsf) is interlaminated clay and silt gradually grading downward to silt and sand with a few dispersed pebbles.

At the Onshore Science Party (OSP), no samples deeper than 49 mbsf were available, as samples had been utilized offshore for either optically stimulated luminescence dating or palynological and sedimentological inspection. However, offshore data reported that very well sorted sand was collected to 68 mbsf, where it changed into sandy silt and became gradu-

ally more like a diamicton. At ~74 mbsf, the Mesozoic (Cretaceous) bedrock was reached.

Unit I

Intervals: 347-M0065A-2H-1, 0 cm, to 4H-1, 58 cm; 347-M0065B-2H-1, 0 cm, to 3H-3, 33 cm; 347-M0065C-2H-1, 0 cm, to 4H-1, 62 cm

Depths: Hole M0065A = 2–9.18 mbsf; M0065B = 3–9.63 mbsf; M0065C = 2–9.22 mbsf

Unit I consists of very well sorted dark greenish gray organic-rich clay with weak lamination by color due to uncommon bioturbation (Fig. F2). The general stratification is overprinted by intervals of black bands with sharp bases. Dispersed shell fragments are found down to the lowermost transition zone with Unit II, where ~10 cm of prominent laminations at the millimeter scale and no bioturbation are found. The boundary with Unit II is gradual.

Smear slide data (see "Core descriptions") show, in general, very low silt and sand contents, remarkable contents of opaque authigenic minerals, and the existence of large centric diatoms. Organic debris is common, possibly algal or plant debris.

The organic-rich clay with bioturbated weak lamination and intervals of black bands is interpreted to indicate general oxic conditions in the marine Holocene sediments of the Bornholm Basin, whereas the lowermost laminated transition zone may represent an initial anoxic phase, similar to the anoxic phases reported in the Eastern Gotland Basin (Zillén and Conley, 2010).

Unit II

Intervals: 347-M0065A-4H-1, 58 cm, to 5H-1, 130 cm; 347-M0065B-3H-3, 33 cm, to 5H-1, 95 cm; 347-M0065C-4H-1, 62 cm, to 5H-2, microbiology sample

Depths: Hole M0065A = 9.18–13.20 mbsf; Hole M0065B = 9.63–13.85 mbsf; Hole M0065C = 9.22 mbsf through microbiology sample

In Unit II, organic content diminishes and the clay is gray to dark gray (Fig. F2). The clay is laminated by color with very fine dark gray iron sulfide–rich laminae at 2–3 mm scale. Downhole, the number of laminae decreases and is substituted by black spots and specks, as well as homogeneous gray intervals. In the lowermost part, a gradual transition to brown clay is observed.

Smear slide studies (see "Core descriptions") show, as with Unit I, typical very low sand and silt contents and fragments of freshwater colonial "lake-dump" diatoms with complete valves of centric diatoms.

Sulfide migration downhole from the upper organic-rich Unit I sediment is a likely example of diagenetic iron sulfidization enhancing Unit II laminations. Alternatively, this migration may be the result of breakdown of primary organic material in the laminations. The smear slide observations of lake-dump diatoms indicate freshwater lake deposition and iron sulfide–laminated clay deeper than the lacustrine Holocene clay that was previously documented as Ancylus Lake sediment (Andrén et al. 2000b).

Unit III

Subunit IIIa

Intervals: 347-M0065A-5H-1, 130 cm, to 12H-1, 105 cm; 347-M0065B-5H-1, 95 cm, to 12H-1, 10 cm; 347-M0065C-5H-2 through microbiology sample

Depths: Hole M0065A = 13.20–36.05 mbsf; Hole M0065B = 13.85–36.10 mbsf; Hole M0065C microbiology sample

Subunit IIIb

Intervals: 347-M0065A-12H-1, 105 cm, to 12H-2, 15 cm; 347-M0065B-12H-1, 10 cm, to 12H-1, 80 cm; Hole M0065C microbiology sample

Depths: Hole M0065A = 36.05–36.65 mbsf; Hole M0065B = 36.10–36.80 mbsf; Hole M0065C microbiology sample

Subunit IIIc

Intervals: 347-M0065A-12H-2, 15 cm, to end of 15H; 347-M0065B-12H-1, 80 cm, through 17S-1; Hole M0065C microbiology sample

Depths: Hole M0065A = 36.65–46.60 mbsf; Hole M0065B = 36.80–49.20 mbsf; Hole M0065C microbiology sample

In Subunit IIIa, the clay color shifts to grayish brown (Fig. F2). The very well sorted clay shows weak lamination by color with a few silt laminae at the millimeter scale. However, the larger intervals are characterized by a massive to contorted (marble structure) appearance. In addition, the unit is characterized by numerous dispersed gray clay/silt intraclasts of millimeter to centimeter scale. Subunit IIIa has a sharp lower boundary. Smear slide studies (see "Core descriptions") show very homogeneous clay with barely any silt and sand content, as well as traces of authigenic minerals characterized by numerous brown flakes, possibly biotite.

Another color change characterizes Subunit IIIb, which consists of dark gray homogeneous clay with weak light–dark color banding and a sharp lower boundary (Fig. F2).

Subunit IIIc, the lowermost subunit, consists of very well sorted grayish brown silty clay with parallel lamination (Fig. F2). Color change on a millimeter to centimeter scale defines the clay lamination, and millimeter-scale silt laminations are common. Downhole, the unit coarsens to a fine to medium sand with laminated silt interbeds and in the lowermost few meters to massive medium-grained sand with few dispersed pebbles.

Smear slide studies (see "Core descriptions") reflect the observed coarsening of grain size. Detrital carbonate is found in all grain sizes up to fine gravel, as well as angular to subrounded quartz sand grains. Reworked foraminifers, rounded oxidized ferromagnesian minerals, and glauconite grains are likewise common.

Unit III is interpreted as a glacial lake deposit. The weak lamination combined with massive and contorted sedimentary structures, as well as clay intraclasts in Subunit IIIa, may be indicative of slumping in an unstable sloping environment with high sedimentation rates. Subunits IIIb and IIIc represent earlier more stable phases of the glaciolacustrine environment. The rhythmically banded clays, increased grain size, and frequency of sand laminations indicate that the lower part is deposited in a more ice-proximal setting.

Biostratigraphy

Diatoms

Hole M0065A was qualitatively analyzed for siliceous microfossils. Unevenly distributed samples were analyzed in Core 347-M0065A-15H (~43 mbsf) (Fig. F3). All 69 diatom taxa found at Site M0065 were identified to species level, with the exception of *Chaetoceros* resting spores, which were recorded if present (Tables T2, T3). Chrysophyte cysts were divided into different morphotypes based on the morphology of their silica cell walls.

The results of the qualitative diatom analyses of Hole M0065A are summarized in a graph showing the number of taxa found divided into different salinity affinities and life forms (planktonic, periphytic, and sea ice) (Fig. F3). Diatoms were classified with respect to salinity tolerance according to the Baltic Sea intercalibration guides of Snoeijs et al. (1993–1998), which divide taxa into five groups: marine, brackish-marine, brackish, brackish-freshwater, and freshwater. Furthermore, if present, other siliceous microfossils found (silicoflagellates, ebridians, and chrysophyte cysts) are recorded (Fig. F3).

2 to ~9 mbsf

The preservation of diatoms is considered poor in this sequence based on the finding of corroded valves and the absence of finely silicified taxa. There is also a high abundance of fractured diatoms and a low overall abundance of diatoms in general throughout this sequence, in accordance with previous studies from the area (Abelmann, 1985; Thulin et al., 1992; Andrén et al., 2000b). Poor preservation may result in overrepresented valves with thick cell walls (e.g., *Paralia sulcata* or the spines of *Pseudosolenia calcar-avis*). This sequence records a brackish-marine assemblage of medium diversity with a high proportion of periphytics. The ice-associated taxon *Fragilariopsis cylindrus* is recorded at one level (Fig. F3).

The silicoflagellate *Dictyocha speculum* and ebridian *Ebria tripartita* are both recorded at two levels, and chrysophyte cysts are recorded with various morphotypes throughout the sequence (Fig. F3).

9–11.4 mbsf

This sequence is dominated by taxa that indicate large lake conditions (i.e., *Aulacoseira islandica*, *Stephanodiscus neoastraea*, *Cocconeis disculus*, *Navicula jentzschii*, *Aneumastus tusculus*, and *Cymatopleura elliptica*) (cf. Hedenström and Risberg 1999). This probably indicates the conditions of the final freshwater phase of the Yoldia Sea stage of Baltic Sea history and/or the Ancylus Lake. These two stages are not easily distinguished in the diatom stratigraphy in the open Baltic Basin because there is no change in salinity (Sohlenius et al., 1996). However, more detailed study with careful diatom counts may show a response to the transgression that defines the transition from the Yoldia Sea stage to Ancylus Lake (Andrén et al., 2011). Abelmann (1985) records high primary production at the beginning of the Ancylus Lake and suggests that the silica supply was high and that valves were less affected by dissolution. A similar observation is made by Andrén et al. (2000b), who found that the preservation of diatoms is good and redeposition of valves less likely. There is no obvious transition (i.e., initial Littorina Sea stage) re-

corded between this sequence and the succeeding brackish-marine sequence.

Chrysophytes are recorded occasionally in this sequence, exclusively as a morphotype with smooth cell walls.

Core depth interval 11.9 mbsf

A single sample records a diatom assemblage with >50% brackish-freshwater and brackish water taxa. It contains a fairly diverse assemblage with both planktonic and periphytic components (e.g., brackish-freshwater *Gyrosigma acuminatum* and *Thalassiosira baltica* and brackish *Brachysira aponina* and *Chamaepinnularia witkowskii*) (Fig. **F3**). This single sample might reflect the brackish phase of the Yoldia Sea stage of Baltic Sea history, but it does not contain the dominance of *T. baltica* that characterizes the assemblage in other parts of the Baltic Basin (cf. Lepland et al., 1999; Paabo, 1985; Andrén et al., 2000a, 2002). According to Abelmann (1985), the Arkona Basin and the southern Bornholm Basin contain no brackish Yoldia Sea stage flora. This is further discussed in Andrén et al. (2000b) in a study from the Bornholm Basin. Because we analyzed a single sample, a more thorough study should be conducted to enable conclusions about the southern extension of the brackish water influence during the Yoldia Sea stage to be drawn.

Core depth interval 12.6 to ~43 mbsf

The lowermost analyzed sequence of Hole M0065A was devoid of siliceous microfossils (Fig. **F3**).

Foraminifers

Results are summarized for the samples taken offshore and onshore (i.e., samples taken from core catchers and regular sections). A total of 55 samples were processed from Holes M0065A, M0065B, and M0065C for the presence of foraminifers (Table **T4**).

Although Sites M0064–M0066 (located in Hanö Bay and Bornholm Basin) are located close to each other, Site M0065 is the only one at which foraminifers occur. Benthic foraminifers occur from the first core (which begins at 2 mbsf) to 8.90 mbsf with the maximum abundance between 3.17 and 6.62 mbsf (common to abundant) (Fig. **F4**). A single foraminifer occurs in Sample 347-M0065A-4H-CC at 12.12 mbsf.

Hanö Bay and Bornholm Basin today have bottom water salinities between 12 and 17 (Samuelsson, 1996), which is intermediate between the salinities of Landsort Deep and Little Belt. The foraminiferal assemblage indeed reflects this, as *Elphidium* spp. still dominate but show more species diversity within the genus. The faunal assemblage is composed of *Elphidium excavatum* f. *clavata*, *Elphidium excavatum* f. *selseyensis*, *Elphidium williamsoni/Elphidium gunteri*, *Elphidium incertum*, and *Haynesina* spp. A similar assemblage was previously described for the Pomeranian Bight, located just southwest of the island of Bornholm (Frenzel et al., 2005).

The highest diversity of species occurs in the same range where the abundance is also highest. This would suggest that bottom water salinity was slightly higher during this time period, which is also in accordance with the ostracod results (see **"Ostracods"**). The occurrence of *Haynesina* sp. around 3.8–4.7 mbsf (Hole M0065B) suggests elevated salinity (~20) compared to the previous and subsequent periods (i.e., more similar to typical assemblages from farther west) (Frenzel et al., 2005; Anjar et al., 2012). When diversity decreases, the remaining species are the *Elphidium* varieties, which are most adapted to harsher conditions.

Ostracods

A total of 52 samples (including 36 core catchers) from Holes M0065A, M0065B, and M0065C were examined for ostracods during the onshore phase of Expedition 347 at the Bremen Core Repository (Germany). Samples were studied in the >125 µm fraction. Ostracods were present in eight samples (Table **T5**).

Ostracod abundance per sediment volume from the three holes varies between 1 and 5 valves per 20 cm^3 sample and up to a maximum abundance of 42 valves per 20 cm^3 at ~8 mbsf (Hole M0065B) (Fig. **F5**). Maximum abundance of foraminifers occurs at ~3–7 mbsf, where common to abundant *Elphidium* tests were recorded (see **"Foraminifers"**). It is possible that salinity changes caused the difference in depths of abundance peaks for foraminifers and ostracods. A total of five taxa were identified for this site: *Palmoconcha* spp., *Robertsonites tuberculatus*, *Cytheropteron latissimum*, *Sarsicytheridea bradii*, and *Paracyprideis* sp.

Palmoconcha spp. is a predominant taxon found in six out of eight samples with ostracods in the interval of 5.73 to 8.88 mbsf (Holes M0065A–M0065C). *Palmoconcha* is a brackish to euhaline genus found at salinities of 10–14 and higher (Frenzel et al., 2010). The uppermost samples at 2.16 mbsf (Hole M0065A) and 3.16 mbsf (Hole M0065B) do not contain this

taxon. *C. latissimum*, *R. tuberculatus*, *S. bradii*, and *Paracyprideis* sp. occur in these samples, indicating higher salinities and an open-sea marine environment.

It is possible that in the interval ~8–9 mbsf salinity is lower and less favorable for foraminifers, such that brackish water ostracods dominate. In the upper part of the record, salinity increases and foraminifers become more abundant, whereas brackish water ostracods decrease in abundance and are replaced with marine species.

Palynological results

Site M0065 is situated in the central part of the southern Baltic Sea. The vegetation of the borderlands in that region belongs to cool temperate forest zone with mixed coniferous and deciduous trees, but the boreal-forest vegetation zone is very close to the site. Palynological analyses for this site focused on Hole M0065A.

Four samples from Hole M0065A were analyzed in total. The two uppermost samples at 2.17 and 8.82 mbsf are characterized by high pollen concentrations (~64,000 and 89,000 pollen grains, respectively), whereas the two other samples (15.78 and 22.63 mbsf) are virtually barren of palynomorphs.

Taxa in samples at 2.17 and 8.82 mbsf are very similar. In both samples, *Pinus sylvestris* type pollen prevails (52% and 53.5%). Among broad-leaved trees, the highest percentages are for *Quercus* pollen (Fig. F6, No. 2): 13% for the sample at 8.82 mbsf and 21% for the one at 2.17 mbsf. *Betula alba* pollen occurs in low abundances: 10% and 6.5%, respectively. In the lower sample (8.82 mbsf), 4% of the total pollen encountered was *Tilia cordata* (Fig. F7).

Age estimates based only on these two pollen spectra are fairly difficult. Because of the location in the center of the southern Baltic Sea and the relatively large distance of Site M0065 to the coast, overrepresentation of *Pinus sylvestris* type and *Picea* pollen (both bisaccate) and far-distance transport from the eastern Baltic region into the site area cannot be ruled out. Fairly high *Quercus* and *Picea* percentages may, however, imply a late Atlantic/Subboreal age for these spectra (Kabailene, 2006). In addition to pollen grains, freshwater algae (e.g., *Botryococcus*) and a mandible of an aquatic insect larva (probably from *Endochironomus*) have been found in the uppermost sample (Fig. F6, No. 1). The only organic-walled dinoflagellate cysts encountered in the uppermost samples belong to the genus *Operculodinium*/*Protoceratium*. The specimens found show particularly short processes. The samples are likely to reflect very minor marine influence.

Geochemistry

Interstitial water

At Site M0065, freshwater and glaciolacustrine deposits are overlain by ~9 m of brackish-marine sediment (see "Lithostratigraphy" and "Biostratigraphy"). Because of safety reasons, the upper ~2 m of the sediment sequence was not sampled (see "Operations"). The brackish-marine deposit in this area is relatively thin compared to those at Sites M0059 and M0063, where they extend to ~47 and 30 mbsf, respectively. The pore water composition reflects a rise in salinity due to the transition from freshwater to brackish-marine conditions (Table T6).

Salinity variations: chloride, salinity, and alkalinity

Concentrations of chloride (Cl^-) are highest near the surface at ~250 mM and then decline to ~20 mM at depth (Fig. F8A). Pore water salinities from shipboard measurements determined with a refractometer and calculated from Cl^- concentrations show good agreement, with salinities derived from both measurements declining from ~15 to 1 across the sampled interval (Table T7; Fig. F8B–F8C). Alkalinity shows a broad maximum of ~40 meq/L from 3 to 10 mbsf, followed by a decline with depth to values of <5 meq/L (Fig. F8D). These results are in line with a transition from freshwater to brackish-marine conditions.

Organic matter degradation: methane, sulfate, sulfide, ammonium, phosphate, iron, manganese, pH, bromide, chloride, and boron

Methane (CH_4) is present to ~36 mbsf in the sediment (Fig. F9A; Table T8). Similar to Sites M0059 and M0063, observed scatter in CH_4 concentrations with depth is probably due to degassing upon core recovery, in particular shallower than ~25 mbsf. Deeper CH_4 concentrations gradually decrease following a smooth profile, suggesting that in this part of the sediment the measurements may reflect actual methane concentrations. Sulfate (SO_4^{2-}) concentrations in the pore water are generally <0.5 mM (Fig. F9B). The presence of sulfide (H_2S; ~0.7 mM) at depths shallower than ~5 mbsf suggests active SO_4^{2-} reduction in the upper part of the sediment (Fig. F9C). Pore water profiles of ammonium (NH_4^+) and phosphate (PO_4^{3-}) (Fig. F9D–F9E) follow the general trend of alkalinity (Fig. F8D), which is consistent with organic matter degradation as a dominant control. Dissolved iron (Fe^{2+}) and manganese (Mn^{2+}) show distinct maxima in the pore water (Fig. F9F–

F9G). Dissolved Fe^{2+} is mostly present in the former lake sediments (with concentrations as high as ~1000 µM), whereas dissolved Mn^{2+} is largely restricted to the brackish-marine sediments and peaks at ~250 µM. Pore water pH decreases from a value of ~8.1 near the surface to a broad minimum of ~7.5 at 17–25 mbsf. Deeper than this depth, pore water pH increases to a value of ~8 and then decreases to ~7.5 again.

The depth profile of dissolved bromide (Br^-) is similar to the chloride (Cl^-) profile, although the profile of Br/Cl does reveal a slight enrichment in pore water Br^- relative to Cl^- with depth (Fig. F10A–F10B). This increase may be linked to release of Br^- during the mineralization of marine organic matter. Dissolved boron (B) decreases from ~375 to 35 µM with depth (Fig. F10C). The maximum in B/Cl in the upper 5–10 m of the sediment may be indicative of release of B from the brackish-marine sediments (Fig. F10D).

Mineral reactions

Sodium, potassium, magnesium, and calcium

Depth profiles of sodium (Na^+), potassium (K^+), and magnesium (Mg^{2+}) resemble those of chloride (Cl^-), suggesting strong control by seawater (Fig. F11A–F11C). The depth profile of Ca^{2+} is distinctly different, however, with a maximum concentration at ~20 mbsf (Fig. F11D). In the upper 10–20 m of the sediment, ratios of Na/Cl, K/Cl, and Mg/Cl (Table T7) are elevated relative to seawater, suggesting release of these cations from the sediment (Fig. F11E–F11G). Low Na/Cl, K/Cl, and Mg/Cl ratios relative to seawater values deeper than 10–20 mbsf may suggest removal of cations to a solid phase. Deeper than ~30 mbsf, salinities are so low that comparison of the ratios is no longer meaningful. Ratios of Ca/Cl in the pore water are always higher than the seawater Ca/Cl ratio and increase strongly downcore. This profile suggests that Ca^{2+} is released from the sediment to the pore water (Fig. F11H), possibly through ion exchange and/or mineral dissolution.

Silica, lithium, barium, and strontium

Concentrations of dissolved silica (H_4SiO_4) and lithium (Li^+) are elevated in the upper 10–15 m of the sediment (Fig. F12A–F12B). This is possibly the result of enhanced mineral weathering or, for H_4SiO_4, dissolution of diatoms in the brackish-marine sediments. A large peak in barium (Ba^{2+}) concentrations is observed between 10 and 20 mbsf, followed by a decline with depth (Fig. F12C). This trend is similar to that observed at Site M0059 and may be due to release of Ba^{2+} from the sediment through ion exchange or mineral dissolution linked to the intrusion of seawater into former freshwater sediments. Pore water strontium (Sr^{2+}) shows a maximum concentration at 20 mbsf, possibly also reflecting release from solid phases (Fig. F12D).

Sediment

Carbon content

The total carbon (TC) content at Site M0065 varies from ~0.4 to 4.4 wt%, with high values in the topmost part of the profile and a pronounced minimum at the transition from freshwater to brackish-marine conditions (Table T9; Fig. F13A). Highest total organic matter (TOC) values (~4 wt%) are observed in the uppermost ~10 m of the investigated profile, possibly suggesting enhanced primary productivity and preservation of organic matter during the deposition of the brackish-marine sediments. The underlying freshwater and glaciolacustrine deposits are characterized by low TOC values that typically do not exceed 0.5 wt% (Table T9; Fig. F13B).

The depth profile of the total inorganic carbon (TIC) content shows minimum values (<0.7 wt%) in the uppermost 15 m of the sediment profile (Table T9; Fig. F13C). Deeper than this depth, the TIC content steadily increases, resulting in values above 3 wt% at the base of the investigated sequence.

Sulfur content

The total sulfur (TS) content ranges from 0.1 to 1.7 wt% (Table T9; Fig. F13D). The generally high TS (>1%) values in the brackish-marine deposits at the core top might be a result of sulfate reduction and the subsequent formation of iron sulfides in the sediments. In contrast, the underlying freshwater and glaciolacustrine sediments, which are characterized by only low sulfate concentrations, generally have TS values varying between 0.10 and 0.14 wt%. Note that the TS content, similar to the TOC content, slightly increases deeper than ~40 mbsf.

Physical properties

This section summarizes the preliminary physical property results from Site M0065. Three holes were drilled at this site. Hole M0065A was drilled to 73.9 mbsf, Hole M0065B to 49.3 mbsf, and Hole M0065C to 47.9 mbsf. Hole M0065C was designated as a microbiology hole and was extensively subsampled onboard (see "Microbiology") prior to any physical properties measurements except Fast-track multisensor core logger (MSCL). For each hole, the uppermost

2 m was washed down to avoid potential chemical contamination (see "Operations"). We focused on the physical property data from Hole M0065A, which has the greatest penetration (Fig. F14), though the core recovery was very low from 46.6 mbsf because of changing coring methods from piston coring to open-hole intervals with spot hammer sampling (see "Operations"). Although all physical property measurements described in "Physical properties" in the "Methods" chapter (Andrén et al., 2015a) were conducted for Site M0065, thermal conductivity data are too sparsely distributed to exhibit any discernable downcore trend.

Natural gamma radiation

High-resolution natural gamma ray (NGR) values are relatively low (<10 cps) and increase progressively from the core top to the lower interval of lithostratigraphic Unit I (Fig. F14; see "Lithostratigraphy"), with few positive excursions observed. These generally low NGR values are interpreted as a result of high water content within organic-rich muds. At the Unit I/II boundary, NGR values decrease and then exhibit increasing values toward the base of lithostratigraphic Unit II (~15 cps). NGR exhibits relatively constant values in lithostratigraphic Subunit IIIa, with several negative excursions from the overall trend that might reflect the presence of silt intraclasts. NGR values decrease slightly (~12 cps) within lithostratigraphic Subunit IIIb. Lithostratigraphic Subunit IIIc is distinguished by gradually decreasing values toward the bottom of the hole. Variability in NGR likely reflects a coarsening-downward sequence from silty clay to medium sand through lithostratigraphic Subunit IIIc.

Shipboard magnetic susceptibility and noncontact resistivity

Magnetic susceptibility is overall generally low (<5 × 10^{-5} SI) and increases slightly toward the base of lithostratigraphic Unit I (Fig. F14). Magnetic susceptibility is higher in lithostratigraphic Unit II and remains relatively constant, except for an abrupt spike (~55 × 10^{-5} SI) observed at ~10 mbsf. The upper interval of lithostratigraphic Subunit IIIa is distinguished by a peak in magnetic susceptibility. However, apart from this peak, magnetic susceptibility remains constant from ~15 mbsf to the base of lithostratigraphic Subunit IIIb. Several positive excursions occurring within lithostratigraphic Subunit IIIa, approximately every 3 m, do not appear to correspond to changes in lithology. With their regular occurrence at approximately the same interval as core runs (~3.3 m), they are possibly an artifact of coring. At the Subunit IIIb/IIIc boundary, magnetic susceptibility increases and then exhibits high and variable values that reflect changes in lithology (increase in silt and sand content; see "Lithostratigraphy").

The noncontact resistivity (NCR) data exhibit a generally similar trend to magnetic susceptibility (Fig. F14). NCR values are very low in lithostratigraphic Units I and II and progressively increase toward the base of lithostratigraphic Subunit IIIa as a normal compaction trend. Similar to magnetic susceptibility, NCR exhibits higher amplitude and more variability in lithostratigraphic Subunit IIIc.

Color reflectance

Color reflectance, in particular a*, reflects downcore changes in lithology (Fig. F14). Lithostratigraphic Units I and II are characterized by low values (more green). At the Unit II/Subunit IIIa boundary, a* values increase sharply and remain high (>4, more red) and constant through lithostratigraphic Subunit IIIa. Values decrease to a mean value of ~1 (greenish) at the Subunit IIIa/IIIb boundary and remain relatively constant in lithostratigraphic Subunits IIIb and IIIc.

Density and *P*-wave velocity

Gamma density was measured at 2 cm intervals during the offshore phase of Expedition 347 (Fig. F15). Gamma density increases progressively from the core top to the base of lithostratigraphic Subunit IIIb. Gamma density exhibits a shift to higher values in Subunit IIIc and remains generally high (~2 g/cm^3) throughout lithostratigraphic Subunit IIIc. Discrete bulk density measurements conducted during the OSP correlate moderately well with the shipboard measurements (r^2 = 0.69; Fig. F16).

P-wave velocity was also measured at 2 cm intervals during the offshore phase of Expedition 347 (Fig. F15). *P*-wave velocity (MSCL) exhibits low and relatively constant values (~1000 m/s) from the core top to ~18 mbsf. Values are higher and highly variable in the middle interval of lithostratigraphic Subunit IIIa (~18–32 mbsf). The lower interval of lithostratigraphic Subunit IIIa, Subunit IIIb, and the upper interval of Subunit IIIc are all characterized by generally more constant values (~1500 m/s), observed in both the MSCL and discrete *P*-wave measurements. From ~39 mbsf to the bottom of Hole M0065A, *P*-wave velocity values are overall higher (>1600 m/s) than the upper section. However, there is a slight decreasing trend from ~39 to ~43 mbsf, where *P*-wave velocity increases again to the bottom of the hole to a high of ~1800 m/s. No significant correlation is observed between the shipboard *P*-wave velocity and the discrete *P*-wave measurements performed during the OSP.

Paleomagnetism

In accordance with the main objectives of the OSP paleomagnetic work, magnetic susceptibility measurements and rudimentary analyses of natural remanent magnetization (NRM) were made on discrete specimens of known volume and mass (see **"Paleomagnetism"** in the "Methods" chapter [Andrén et al., 2015a]). Discrete samples were taken from Holes M0065A (89 specimens), M0065B (19 specimens), and M0065C (9 specimens) for a total of 117 samples. Magnetic susceptibility ranges between 0.03 × 10^{-6} and 0.43 × 10^{-6} m^3/kg through the sequence, with values greater than 0.2 × 10^{-6} m^3/kg confined to Subunit IIIc (an interval varying from coarse fine to medium sand) and the upper part (16–13 mbsf) of Subunit IIIa. Paleomagnetic pilot samples recovered from Units I and II, considered to be Holocene in age, have inclinations that are consistent with the geocentric axial dipole (GAD) inclination value (i.e., 71°). The pilot samples located in Subunit IIIc, which is likely to be late glacial and contains slumped material, are characterized by poor magnetic stability, and this unit contains scattered inclination values between 0° and 30°.

Discrete sample measurements

A total of 117 discrete samples were obtained from Holes M0065A and M0065C. Samples were recovered at intervals of ~50 cm from inside the site splice.

Magnetic susceptibility

The results of the magnetic analyses are shown in Figure **F17.** Magnetic susceptibility (χ), which was normalized to sample mass, ranges between 0.03 × 10^{-6} and 0.43 × 10^{-6} m^3/kg. Samples taken from Subunits IIIc and IIIb have χ values between 0.1 × 10^{-6} and 0.43 × 10^{-6} m^3/kg. The overlying Subunit IIIa has χ values between ~0.1 × 10^{-6} and 0.15 × 10^{-6} m^3/kg, with a distinct peak at depths between 16 and 13 mbsf of 0.1 × 10^{-6} and 0.3 × 10^{-6} m^3/kg.

The χ of Unit II is variable and includes one interval (13–10 mbsf) in which the values decrease upcore from ~0.1 × 10^{-6} to 0.05 × 10^{-6} m^3/kg. From 10 mbsf to the top of the core (i.e., at ~2 mbsf; Unit I), values of χ are <0.1 × 10^{-6} m^3/kg and are relatively constant.

Sediment wet density and χ are not related to each other, although χ ranges over half an order of magnitude, which suggests that changes in the magnetic mineralogy and/or grain size are determining χ. Two trends are apparent in the biplot of χ versus NRM intensity, one that indicates high χ/NRM ratios and one that indicates low χ/NRM ratios. The samples from Subunit IIIc have high χ/NRM ratios.

Natural remanent magnetization and its stability

Results of the pilot sample demagnetization (Fig. **F18**) indicate that an alternating field (AF) of 5 mT is sufficient to remove a weak viscous remanent magnetization (VRM). Four different responses to the sequential AF demagnetization are displayed by samples from Site M0065. Category 1 includes the samples of the grayish brown silty clay with planar lamination that characterizes Subunit IIIc, and they lose 50% of their NRM intensity at AF <15 mT, with a small residual component left at 40 mT that is unaffected by more intense demagnetization levels. The univectorial diagram does not trend to the origin of the diagram. Category 2, which includes a sample from Subunit IIIa at 23.52 mbsf, is typified by a paleomagnetic vector that is moderately "hard," indicating high coercivity and demagnetized up to the maximum AF demagnetization level of 80 mT, with a vector that trends toward the origin of the orthogonal projection. Category 3 has a "softer" magnetic behavior, with the removal of a significant viscous remanence at the 5 mT AF demagnetization level. The sample demagnetizes relatively easily and loses 50% of its magnetization between 30 and 40 mT. It is univectorial and trends to the origin of the orthogonal plot. Category 4 shows the behavior of a specimen that is characterized by low coercivity and a quite "soft" behavior of demagnetization. About 50% of the magnetization is removed by 20 mT, and the univectorial diagram shows a distinct linear behavior, trending toward the origin of the diagram.

After removal of the viscous overprint the NRM intensity of the samples recovered from Site M0065 lies in the range between 0.07 × 10^{-3} and 150 × 10^{-3} A/m and there is a positive relationship with χ in Subunits IIIa, IIIb, and IIIc, in which large peaks in NRM intensity are reflected in the χ data, and also in Units II and I (Fig. **F17**).

Paleomagnetic directions

The directions of the paleomagnetic vectors are illustrated by the inclination data in Figure **F17.** The inclination data from Unit III are scattered, with many positive shallow values and few negative values. Only two samples from these three units approach the GAD prediction for this site location. In contrast, the inclination data from Units II and I group closer to the GAD prediction, but there is a bias toward

higher values (i.e., between 14 to 12 mbsf spanning the boundary between Subunit IIIa and Unit II). It is notable that the samples taken from 10 to 2 mbsf Unit I, which have relatively low χ values, plot within a few degrees of the GAD prediction. The variable magnetic properties downhole and different categories of response to AF demagnetization probably preclude using the paleomagnetic data for relative dating purposes.

Microbiology

Hole M0065C was drilled specifically for microbiology, interstitial water chemistry, and unstable geochemical parameters at Site M0065. Counts of microbial cells were made by fluorescence microscopy using the acridine orange direct count (AODC) method and by flow cytometry (FCM) using SYBR green DNA stain during the OSP. Further counts by fluorescence microscopy will be conducted after the OSP using both acridine orange and SYBR green staining.

A total of 15 sediment samples were counted for microbial cell numbers on the ship and during the OSP (Table **T10**). Of these, 11 samples were enumerated using the flow cytometer, and all 15 samples were enumerated using the epifluorescence microscope counting technique.

The most striking observations for these data are that cell counts by AODC are extremely high in Unit I and that the two cell counting techniques do not produce similar results in the upper half of this hole (Fig. **F19;** see **"Microbiology"** in the "Site M0063" chapter for a similar pattern of results [Andrén et al., 2015b]). The uppermost cell count at 3.53 mbsf, by FCM, was 9.42×10^8 cells/cm^3, whereas 1.23×10^{10} cells/cm^3 were determined by AODC, a 13-fold difference. In the lower half of this hole, data from both counting techniques appeared similar. The minimum microbial populations were determined as 7.10×10^7 cells/cm^3 at 23.33 mbsf by FCM and 6.18×10^7 cells/cm^3 at 13.43 mbsf by AODC.

Regression analyses of both data profiles indicated different trends shallower and deeper than ~12 mbsf (Fig. **F19**). The decrease in cell numbers with depth was significantly steeper shallower than this depth compared to deeper than this depth both for FCM ($F = 8.67$; degree of freedom [df] = 1.7; $P < 0.025$) and for AODC ($F = 45.82$; df = 1.11; $P << 0.001$). In the upper 12 m the change in cell numbers with depth was approximately 2.3 times steeper for AODC compared to FCM. This compares to a difference of 2.4 times steeper in Hole M0063E (see **"Microbiology"** in the "Site M0063" chapter [Andrén et al., 2015b]). Deeper than 12 mbsf, regression lines from the two depth profiles were not significantly different from each other ($F = 0.577$; df = 1.11 [not significant]), which was confirmed by a paired sample t-test ($t = 0.598$; df = 6 [not significant]).

This is the same situation that was encountered in samples from Hole M0063E where in the upper part of the hole many of the cells were aggregated in clumps of "fluff," making accurate enumeration by either method difficult or impossible (see interpretation in **"Microbiology"** in the "Site M0063" chapter [Andrén et al., 2015b]), and this resulted in significant underestimation of cell numbers by FCM compared to AODC. An improved processing technique will need to be developed to deal with these samples, and it is possible that even higher concentrations of cells will be detected than already reported for this hole. The fluff is possibly bacterially derived exopolysaccharide causing cell clumping, and it is of note that this depth interval of difficult-to-count samples coincides with both the largest differences between the two counting techniques and the presence of organic-rich sediment (see **"Geochemistry";** Figs. **F13A, F19**).

The profile break at 12 mbsf does seem to be related to sediment column stratigraphy, as this depth roughly correlates with the transition between the upper brackish-marine sediments and the lower late glacial lake clay deposits at the Unit II/III boundary. In the organic-rich sediments shallower than 12 mbsf, bacterial degradation of organic matter has produced a broad maximum in alkalinity that reaches 38 meq/L in the upper part of the hole compared to 4–5 meq/L in the lower half of the hole (see **"Geochemistry"**). The high cell numbers thus coincide with the interval of high degradation rate of organic matter. Conversely, salinity decreases more or less linearly from the sediment surface to ~30 mbsf and does not appear related to the cell profiles (Fig. **F19**).

As was reported for Sites M0059, M0060, M0061, and M0063, cell numbers were very high and, with one exception, all cell counts exceeded the upper prediction limit for the global regression (Fig. **F19**). The maximum deviation from the global regression was at 29.93 mbsf for the FCM profile with a 36-fold higher cell number, whereas for the AODC technique the greatest deviation was at 6.83 mbsf with a 370-fold higher number. It is of note that the cell density of 1.23×10^{10} cells/cm^3 at 3.53 mbsf is among the highest observed in all marine sediments examined by scientific drilling.

When the data from both techniques are plotted against each other, results from deeper than 12 mbsf

cluster around the line of x = y (Fig. F20). Data are too clustered for a regression line to be calculated and compared to the x = y line. Results from shallower than 12 mbsf clearly deviate from the x = y line with higher numbers obtained by the AODC method.

Perfluorocarbon (PFC) tracer was detected in the liner fluid and exteriors of all cores, indicating continuous PFC delivery into the microbiology borehole (Table T11). Liner fluid PFC concentrations varied over 1–2 orders of magnitude (Fig. F21A), indicating variations in the rates of PFC delivery and mixing into the drilling fluid stream. Most of the measured PFC concentrations were below the target concentration of 1 mg PFC/L. Nonetheless, the liner fluid PFC concentrations are on average considerably higher than at the other three sites, remaining above 10^{-5} g PFC/L in all samples (apart from Core 2H) and in two cores (347-M0065C-3H and 4H) closely approaching the PFC target concentration. PFC was above detection in all core halfway samples and all but two interior samples (Cores 6H and 7H; Fig. F21B). As at Sites M0059 and M0060, contamination was relatively highest in the uppermost part of the hole (Core 347-M0065C-2H) and showed no depth- or lithology-related trend below (Figs. F19, F21C). Remarkably, PFC contamination was 2–3 orders of magnitude higher in several "core halfway" sections than core exteriors (Cores 7H, 10H, and 12H), a phenomenon that was only observed once across the three other microbiology sites (Core 347-M0063E-23H).

Compared to the other sites, Site M0065 has a higher fraction of cores that are suitable for microbiological analyses. No contamination could be detected in interiors of Cores 347-M0065C-6H and 7H. Moreover, Core 3H only showed marginal evidence of contamination, despite having the highest PFC concentration in the liner fluid of all cores, and Cores 9H, 10H, and 12H were calculated to have potentially fewer than 100 contaminant cells/cm^3 in core interiors (Table T11; Fig. F21D).

Stratigraphic correlation

At Site M0065 three holes were drilled: Holes M0065A (73.9 mbsf), M0065B (49.3 mbsf), and M0065C (47.9 mbsf). The uppermost 2 m of sediment was open holed at each location because of the possibility of chemical contamination in surface sediments (see "Operations"). Hole M0065C was a microbiology hole, and core material was partly consumed by subsampling to 34 meters composite depth (mcd). Composite depths for Site M0065 were based on correlation of magnetic susceptibility (Fig. F22). The correlation was checked against scanned core slab images as well as sedimentology, and continuity of the composite record was checked against downhole log data. All major features from Hole M0065A were correlated to downhole log data (Fig. F23). Based on this, within the uppermost 47.5 mcd, correlation was possible within a 0.1 m error margin. The depth offsets that define the composite section for Site M0065 are given in Table T12 (affine table). No compression or expansion corrections were applied to the data.

It was possible to construct one continuous splice for Site M0065 to 47.5 mcd (Table T13). Deeper core material was sampled for optically stimulated luminescence but was not logged through the MSCL because of the hammer sampling coring method acquiring very little core material.

Seismic units

Seismic sequence boundary-sediment core-MSCL log (magnetic susceptibility) correlations are shown in Figure F24. Two-way traveltime values for each lithostratigraphic unit boundary were calculated using sound velocity values measured during the OSP (*z*-axis velocities, see "Physical properties") (Table T14). Correlations are based on the integration of seismic data and lithostratigraphy (see "Lithostratigraphy"). Uncertainties in the time-depth function could have resulted in minor inconsistencies between seismic features, sedimentological observations from cores, and MSCL logs.

Seismic Unit I

Two-way traveltime: 0.128 ms

Lithology: organic-rich dark greenish clay with weak laminations (lithostratigraphic Unit I)

Depth: 2.00–9.18 mbsf (M0065A), 3.00–9.63 mbsf (M0065B), 2.00–9.22 mbsf (M0065C)

Unit I corresponds to the seismic unit that is transparent and weakly stratified. In sediment cores, this unit displays low magnetic susceptibility values.

Seismic Unit II

Two-way traveltime: 0.134 ms

Lithology: laminated gray to dark gray clay (lithostratigraphic Unit II)

Depth: 9.18–13.20 mbsf (M0065A), 9.63–13.85 mbsf (M0065B),

Unit II shows increasing magnetic susceptibility values downcore. A distinctive spike at 10 mbsf may indicate the presence of greigite (Fe_3S_4) magnetofossils, which have been reported from different various sites in the Baltic Sea (Reinholdsson et al., 2013). In the seismic profile, this spike corresponds to a well-

defined reflector. This seismic unit is crudely stratified.

Seismic Unit III

Seismic Subunit IIIa

Two-way traveltime: 0.168 ms
Lithology: grayish brown laminated clay, massive to contorted (lithostratigraphic Subunit IIIa)
Depth: 13.20–36.05 mbsf (M0065A), 13.85–36.10 mbsf (M0065B)

Seismic Subunit IIIa shows slight rhythmic variations in magnetic susceptibility values. It also shows somewhat irregular internal structures, which could be related to deformation of originally laminated clay.

Seismic Subunit IIIb

Two-way traveltime: 0.169 ms
Lithology: dark gray laminated clay (lithostratigraphic Subunit IIIb)
Depth: 36.05–36.65 mbsf (M0065A), 36.10–36.80 mbsf (M0065B)

Seismic Subunit IIIb is difficult to correlate with a well-defined seismic unit. However, it approximately coincides with the strong reflector at the transition from seismic Unit III to seismic Unit IV.

Seismic Unit IV

Two-way traveltime: 0.182 ms
Lithology: laminated grayish brown silt and clay with sand content increasing downcore. The lowermost few meters consist of massive sand (lithostratigraphic Subunit IIIc)
Depth: 36.65–46.60 mbsf (M0065A), 36.80–49.20 mbsf (M0065B)

Unit IV is characterized by high magnetic susceptibility values that are quite variable, possibly reflecting variations in sand and silt content within the laminated fine-grained unit. In the seismic profile, the upper boundary of Unit IV roughly corresponds to a very strong reflector. In the lower part of Unit IV, several nonparallel reflectors can be seen and the unit seems to continue further down.

Downhole measurements

Logging operations

Hole M0065A

Hole M0065A was drilled to 73.9 m drilling depth below seafloor (DSF). In preparation for logging, the hole was circulated with seawater and the drill string was pulled back in the hole to 14 m wireline log depth below seafloor (WSF). Logging operations started in Hole M0065A with rigging up the Weatherford logging setup.

For downhole logging in Hole M0065A, two tool strings were deployed:

- gamma ray tool (MCG)/array induction tool (MAI) tool string, measuring natural gamma ray and electrical resistivity, and
- MCG/spectral gamma ray tool (SGS) tool string, measuring total gamma ray and spectral gamma ray.

The MCG/MAI tool string was lowered and downlogged to 41 m WSF. The hole was then uplogged to the seafloor. The tools provided continuous and good quality log data. The wireline depth to the seafloor was determined from the step increase in gamma ray values.

After this, the MCG/SGS tool string was lowered and reached only ~16 m WSF while downlogging.

The decision was taken to run in the hole with the drill pipe again to ~45 m DSF and do a wiper-trip of the hole. After this, the tool string with total gamma ray and spectral gamma ray was deployed again but only reached ~20 m WSF. After this unsuccessful attempt, logging operations were abandoned.

Hole M0065C

Hole M0065C was drilled to 47.9 m DSF. In preparation for logging, the hole was circulated with seawater and the drill string was pulled back in the hole to 13.2 m WSF. Logging operations started in Hole M0065C with rigging up the Weatherford logging setup.

For downhole logging in HoleM0065C, two tool strings were deployed:

- MCG/SGS/sonic sonde (MSS) tool string, measuring natural gamma ray, spectral gamma ray, and sonic velocity, and
- MCG/microimager (CMI) tool string, measuring total gamma ray and high-resolution electrical images.

The MCG/SGS/MSS tool string was lowered and downlogged to 40 m WSF. The hole was then uplogged to the seafloor. The tools provided continuous and good quality log data. The wireline depth to the seafloor was determined from the step increase in gamma ray values.

The MCG/CMI tool string was lowered to 40 m WSF with the calipers closed. The hole was then uplogged with open calipers at high resolution.

Hole M0065A logging units

Hole M0065A is divided into five units on the basis of the logs (Fig. F25). The uplog was used as the reference to establish the wireline log depth below seafloor depth scale.

Logging Unit 1: base of drill pipe to 20 m WSF

Logging Unit 1 is characterized by high values in NGR between 100 and 120 gAPI indicating high clay content. Resistivity is constantly increasing through this unit as a normal compaction trend.

Logging Unit 2: from 20 to 26 m WSF

After a sudden drop of NGR at 20 m WSF, natural gamma ray values slightly increase again with depth showing some large fluctuations at 23 m WSF. Resistivity is constantly increasing. The sudden drop in NGR can be explained by the clay/silt intraclasts as described in "Lithostratigraphy" for Subunit IIIa.

Logging Unit 3: from 26 to 34.1 m WSF

After a negative excursion at 26 m WSF and large fluctuations between 26 and 28 m WSF, NGR shows constantly high values through this logging unit. Resistivity increases with depth at a constant rate. Again these fluctuations can be due to the presence of clay/silt intraclasts.

Logging Unit 4: from 34.1 to 37.1 m WSF

NGR is characterized by large changes in this logging unit. Between 35 and 36 m WSF, NGR values are very high after a minimum of 60 gAPI at 34.1 m WSF. NGR shows a sudden drop again at 37.1 m WSF. Resistivity shows some oscillation in this logging unit but still generally increases with depth.

Logging Unit 5: from 37.1 to 41 m WSF

Logging Unit 5 is characterized by an increase in NGR after the natural gamma ray values dropped to 60 gAPI at 37.1 m WSF. Resistivity values are slightly decreasing and show invasion of bore fluid into the formation.

Hole M0065C logging units

Hole M0065C is divided into two units on the basis of the logs (Fig. F26). The uplog was used as the reference to establish the wireline log depth below seafloor depth scale.

Logging Unit 1: base of drill pipe to 18 m WSF

Logging Unit 1 is characterized by a constantly decreasing natural gamma ray. The sonic log stays constant in this logging unit. This decrease in NGR could correspond to the diminished organic content in lithostratigraphic Unit II (see "Lithostratigraphy").

Logging Unit 2: 18–40 m WSF

In logging Unit 2, NGR values are constant with some fluctuations, possibly caused by the clay/silt intraclasts (lithostratigraphic Subunit IIIa; see "Lithostratigraphy"). There are no major changes in the sonic log. The calipers show that borehole conditions were very poor in this last logging unit.

References

Abelmann, A., 1985. Palökologische und ökostratigraphische Untersuchungen von Diatomeenassoziationen an holozänen Sedimenten der zentralen Ostsee [Ph.D. thesis]. Univ. Kiel, Germany.

Andrén, E., Andrén, T., and Kunzendorf, H., 2000a. Holocene history of the Baltic Sea as a background for assessing records of human impact in the sediments of the Gotland Basin. *Holocene,* 10(6):687–702. **doi:10.1191/09596830094944**

Andrén, E., Andrén, T., and Sohlenius, G., 2000b. The Holocene history of the southwestern Baltic Sea as reflected in a sediment core from the Bornholm Basin. *Boreas,* 29(3):233–250. **doi:10.1111/j.1502-3885.2000.tb00981.x**

Andrén, T., Björck, S., Andrén, E., Conley, D., Zillén, L., and Anjar, J., 2011. The development of the Baltic Sea Basin during the last 130 ka. *In* Harff, J., Björck, S., and Hoth, P. (Eds.), *Central and Eastern European Development Studies (CEEDES): The Baltic Sea Basin:* Berlin (Springer-Verlag), 75–97. **doi:10.1007/978-3-642-17220-5_4**

Andrén, T., Jørgensen, B.B., Cotterill, C., Green, S., Andrén, E., Ash, J., Bauersachs, T., Cragg, B., Fanget, A.-S., Fehr, A., Granoszewski, W., Groeneveld, J., Hardisty, D., Herrero-Bervera, E., Hyttinen, O., Jensen, J.B., Johnson, S., Kenzler, M., Kotilainen, A., Kotthoff, U., Marshall, I.P.G., Martin, E., Obrochta, S., Passchier, S., Quintana Krupinski, N., Riedinger, N., Slomp, C., Snowball, I., Stepanova, A., Strano, S., Torti, A., Warnock, J., Xiao, N., and Zhang, R., 2015a. Methods. *In* Andrén, T., Jørgensen, B.B., Cotterill, C., Green, S., and the Expedition 347 Scientists, *Proc. IODP,* 347: College Station, TX (Integrated Ocean Drilling Program). **doi:10.2204/iodp.proc.347.102.2015**

Andrén, T., Jørgensen, B.B., Cotterill, C., Green, S., Andrén, E., Ash, J., Bauersachs, T., Cragg, B., Fanget, A.-S., Fehr, A., Granoszewski, W., Groeneveld, J., Hardisty, D., Herrero-Bervera, E., Hyttinen, O., Jensen, J.B., Johnson, S., Kenzler, M., Kotilainen, A., Kotthoff, U., Marshall, I.P.G., Martin, E., Obrochta, S., Passchier, S., Quintana Krupinski, N., Riedinger, N., Slomp, C., Snowball, I., Stepanova, A., Strano, S., Torti, A., Warnock, J., Xiao, N., and Zhang, R., 2015b. Site M0063. *In* Andrén, T., Jørgensen, B.B., Cotterill, C., Green, S., and the Expedition 347 Scientists, *Proc. IODP,* 347: College Station, TX

(Integrated Ocean Drilling Program). doi:10.2204/iodp.proc.347.107.2015

Andrén, T., Lindeberg, G., and Andrén, E., 2002. Evidence of the final drainage of the Baltic Ice Lake and the brackish phase of the Yoldia Sea in glacial varves from the Baltic Sea. *Boreas,* 31(3):226–238. doi:10.1111/j.1502-3885.2002.tb01069.x

Anjar, J., Adrielsson, L., Bennike, O., Björck, S., Filipsson, H.L., Groeneveld, J., Knudsen, K.L., Larsen, N.K., and Möller, P., 2012. Palaeoenvironments in the southern Baltic Sea Basin during marine isotope Stage 3: a multi-proxy reconstruction. *Quat. Sci. Rev.,* 34:81–92. doi:10.1016/j.quascirev.2011.12.009

Frenzel, P., Keyser, D., and Viehberg, F.A., 2010. An illustrated key and (palaeo)ecological primer for postglacial to Recent Ostracoda (Crustacea) of the Baltic Sea. *Boreas,* 39(3):567–575. doi:10.1111/j.1502-3885.2009.00135.x

Frenzel, P., Tech, T., and Bartholdy, J., 2005. Checklist and annotated bibliography of recent Foraminiferida from the German Baltic Sea coast. *Stud. Geol. Pol.,* 124:67–86. http://sgp.ing.pan.pl/124_pdf/SGP124_067-086.pdf

Hedenström, A., and Risberg, J., 1999. Early Holocene shore-displacement in southern central Sweden as recorded in elevated isolated basins. *Boreas,* 28(4):490–504. doi:10.1111/j.1502-3885.1999.tb00236.x

Kabailienė, M., 2006. Late Glacial and Holocene stratigraphy of Lithuania based on pollen and diatom data. *Gelogija,* 54(2):42–48.

Lepland, A., Heinsalu, A., and Stevens, R.L., 1999. The pre-Littorina diatom stratigraphy and sediment sulphidisation record from the west-central Baltic Sea: implications of the water column salinity variations. *GFF,* 121(1):57–65. doi:10.1080/11035899901211057

Paabo, K., 1985. Diatomological studies of two cores from the Western Baltic. *Striae,* 23:83–91.

Reinholdsson, M., Snowball, I., Zillén, L., Lenz, C., and Conley, D.J., 2013. Magnetic enhancement of Baltic Sea sapropels by greigite magnetofossils. *Earth Planet. Sci. Lett.,* 366:137–150. doi:10.1016/j.epsl.2013.01.029

Roussel, E.G., Cambon Bonavita, M.-A., Querellou, J., Cragg, B.A., Webster, G., Prieur, D., and Parkes, J.R., 2008. Extending the sub-sea-floor biosphere. *Science,* 320(5879):1046. doi:10.1126/science.1154545

Samuelsson, M., 1996. Interannual salinity variations in the Baltic Sea during the period 1954–1990. *Cont. Shelf Res.,* 16(11):1463–1477. doi:10.1016/0278-4343(95)00082-8

Snoeijs, P., Vilbaste, S., Potapova, M., Kasperoviciene, J., and Balashova, J. (Eds.), 1993–1998. *Intercalibration and Distribution of Diatom Species in the Baltic Sea* (Vol. 1–5): Uppsala, Sweden (Opulus Press).

Sohlenius, G., Sternbeck, J., Andrén, E., and Westman, P., 1996. Holocene history of the Baltic Sea as recorded in a sediment core from the Gotland Deep. *Mar. Geol.,* 134(3–4):183–201. doi:10.1016/0025-3227(96)00047-3

Thulin, B., Possnert, G., and Vuorela, I., 1992. Stratigraphy and age of two postglacial sediment cores from the Baltic Sea. *GFF,* 114(2):165–180. doi:10.1080/11035899209453882

Zillén, L., and Conley, D.J., 2010. Hypoxia and cyanobacterial blooms are not natural features of the Baltic Sea. *Biogeosci. Discuss.,* 7(2):1783–1812. doi:10.5194/bgd-7-1783-2010

Publication: 20 February 2015
MS 347-109

Figure F1. Graphic lithology log summary. Depths given represent lithostratigraphic boundaries in Holes M0065A (top of Unit 1 to top of Subunit IIIc) and M0065B (base of Subunit IIIc).

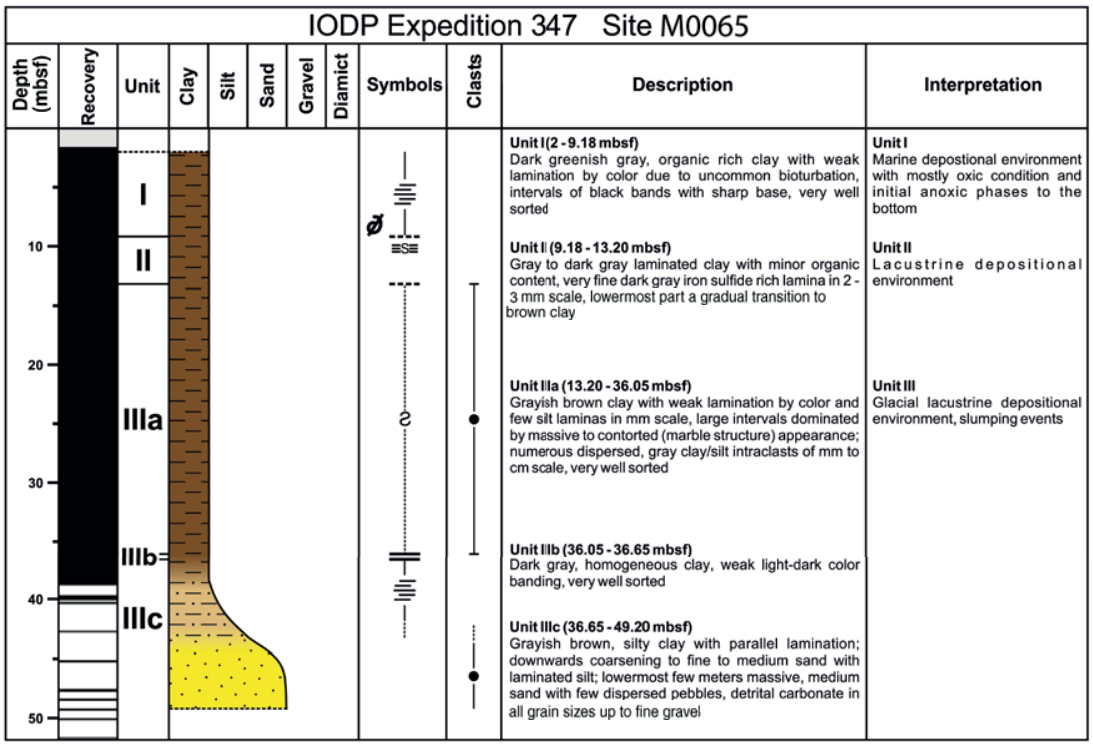

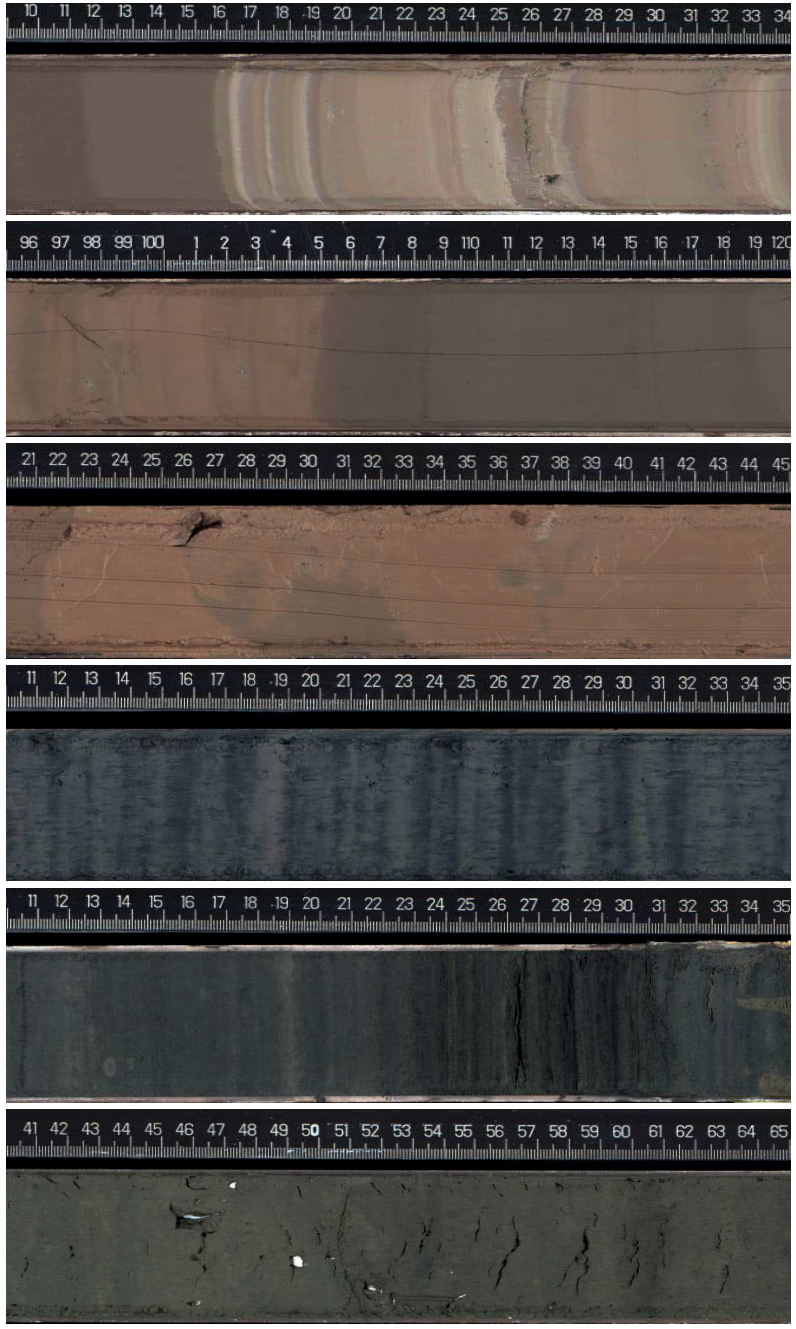

Figure F2. Examples of lithostratigraphic units, Hole M0065A. **A.** Unit I. **B.** Unit I. **C.** Unit II. **D.** Subunit IIIa. **E.** Subunit IIIb. **F.** Subunit IIIc.

Figure F3. Analyzed levels and the relative proportion of diatom taxa showing different salinity requirements, Hole M0065A. Presence of sea ice related taxa and other siliceous microfossils recorded in the cores (red dots), as well as the number of taxa with planktonic and periphytic life forms, are also presented. Siliceous microfossil data are only qualitative presence/absence data and should be interpreted cautiously until quantitative data are generated.

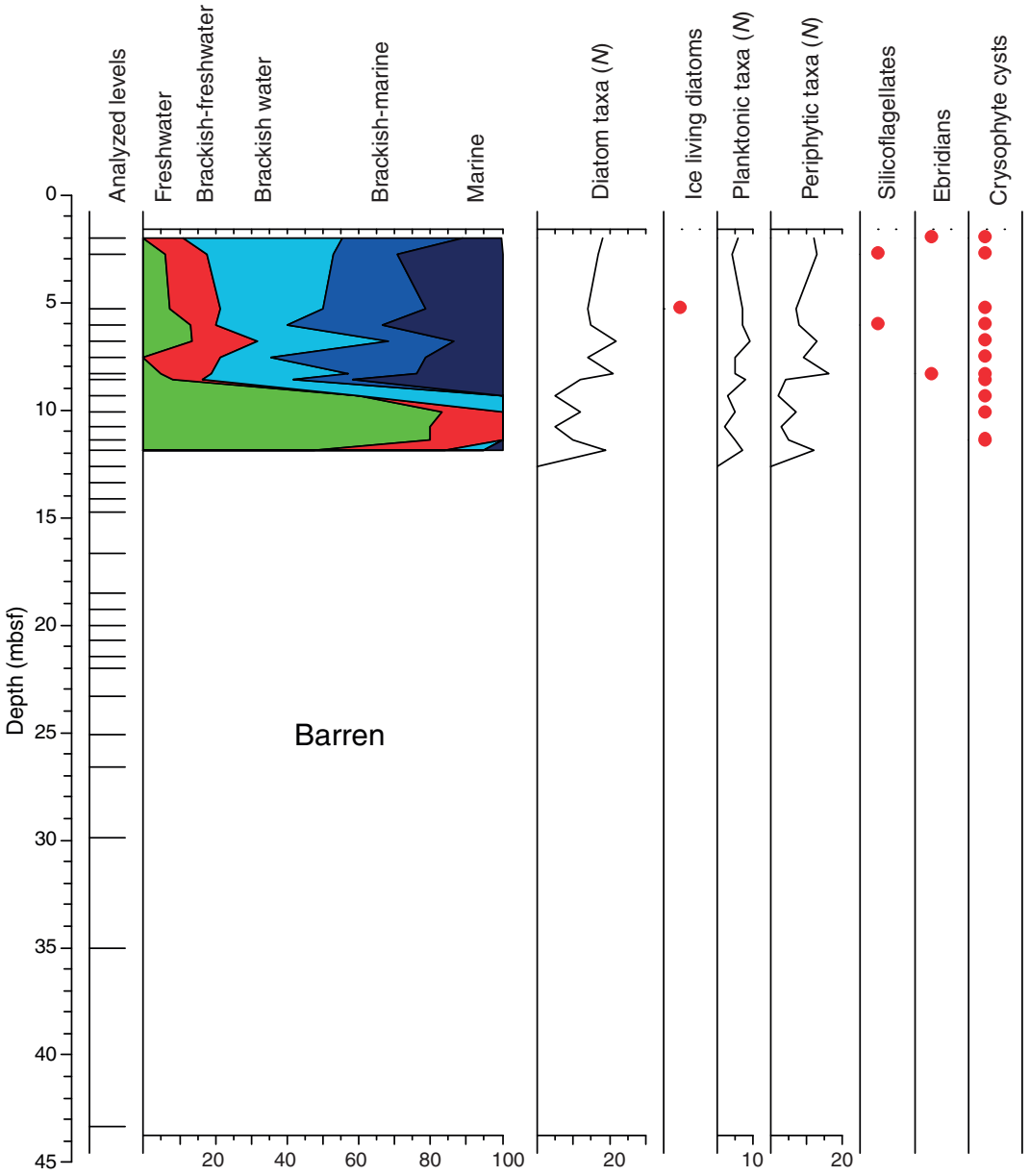

Figure F4. Abundance of benthic foraminifers based on the abundance classification defined in the **"Methods"** chapter (Andrén et al., 2015a), Site M0065. Increasing shading indicates abundances sufficient for faunal and/or geochemical analyses.

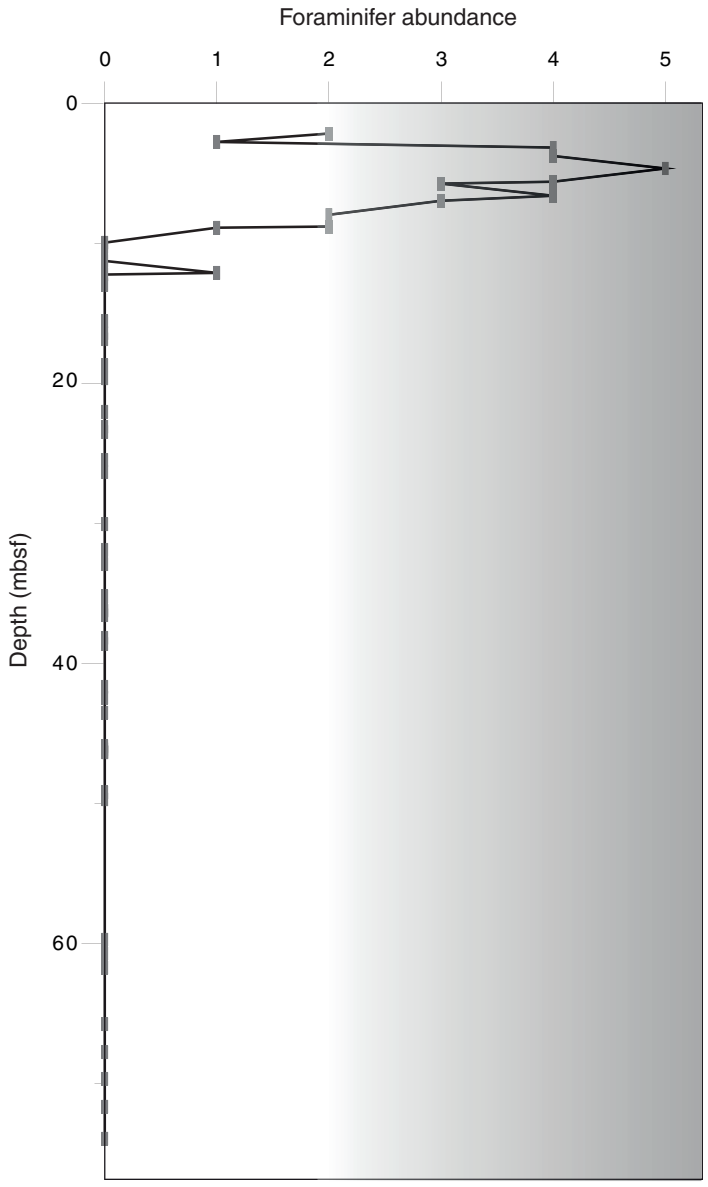

Figure F5. Ostracod abundance per sediment volume, Site M0065.

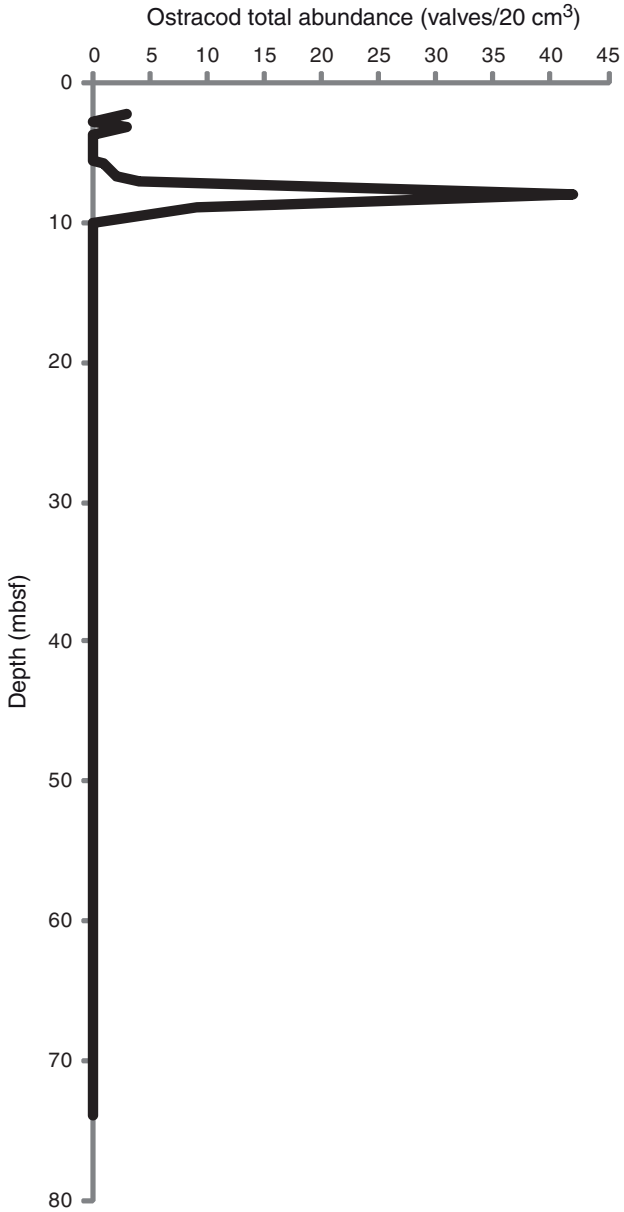

Figure F6. Palynomorphs encountered in Core 347-M0065A-2H. **1.** Chironomid jaw. **2.** *Quercus* pollen grain. Scale bars = 20 µm.

Figure F7. Pollen diagram with bisaccate pollen included in the reference sum, Hole M0065A. For all samples included in the diagram, >100 pollen grains have been counted.

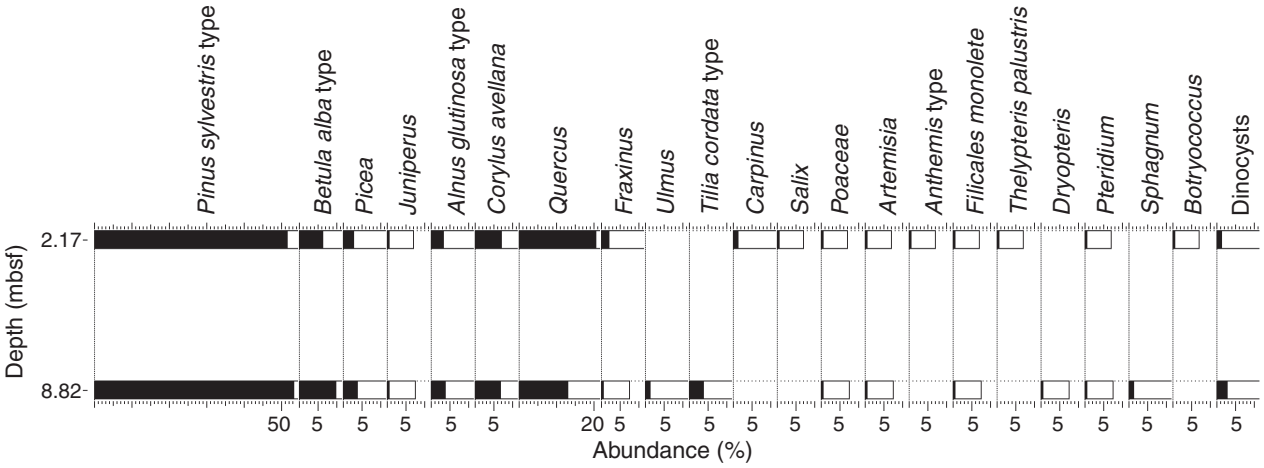

Figure F8. Concentrations of (**A**) chloride, (**B**) salinity by refractometer, (**C**) chloride-based salinity, and (**D**) alkalinity in interstitial water samples, Site M0065.

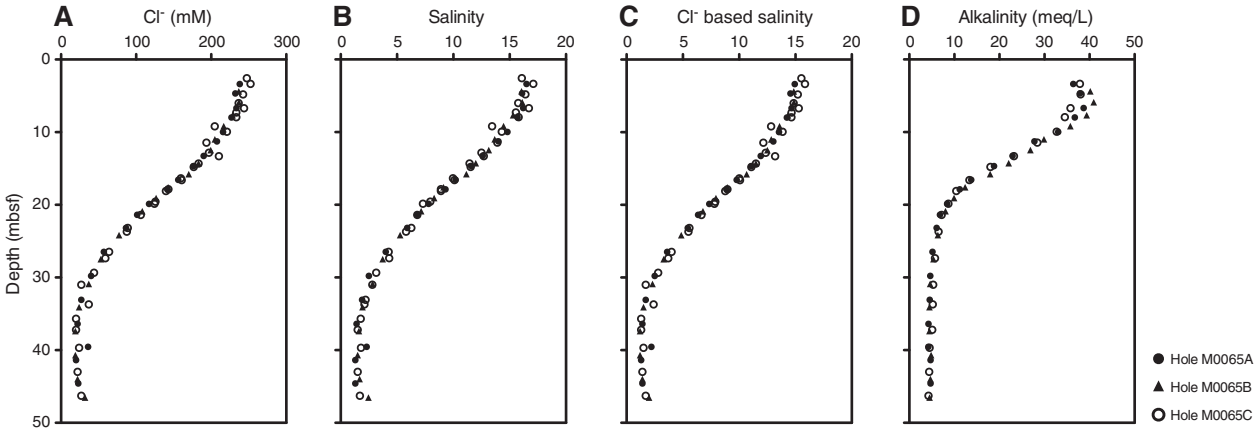

Figure F9. Concentrations of (**A**) methane, (**B**) sulfate, (**C**) sulfide, (**D**) ammonium, (**E**) phosphate, (**F**) iron, (**G**) manganese, and (**H**) pH from interstitial water samples, Site M0065.

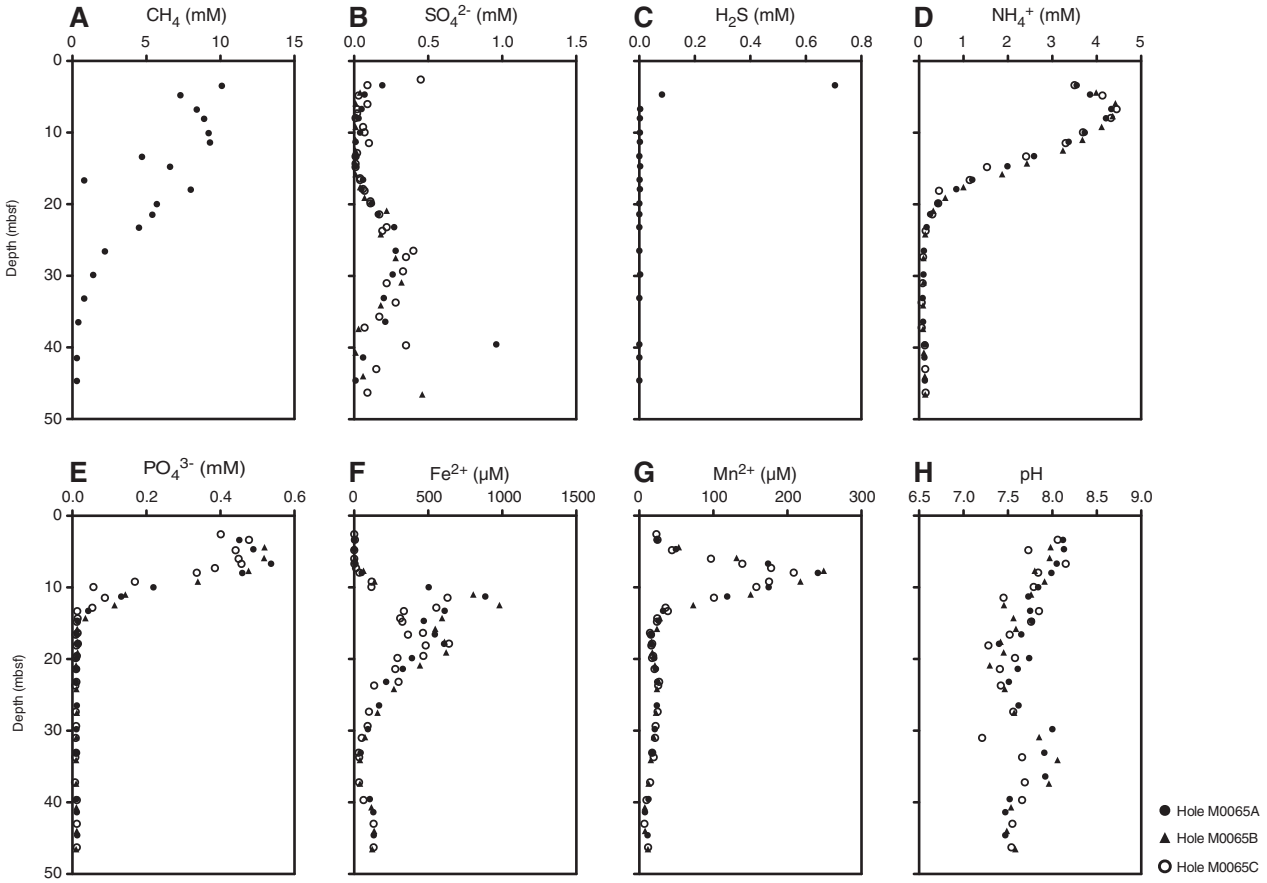

Figure F10. Concentrations and ratios of (**A**) bromide, (**B**) bromide/chloride, (**C**) boron, and (**D**) boron/chloride from interstitial waters samples, Site M0065. Dashed lines = seawater ratio.

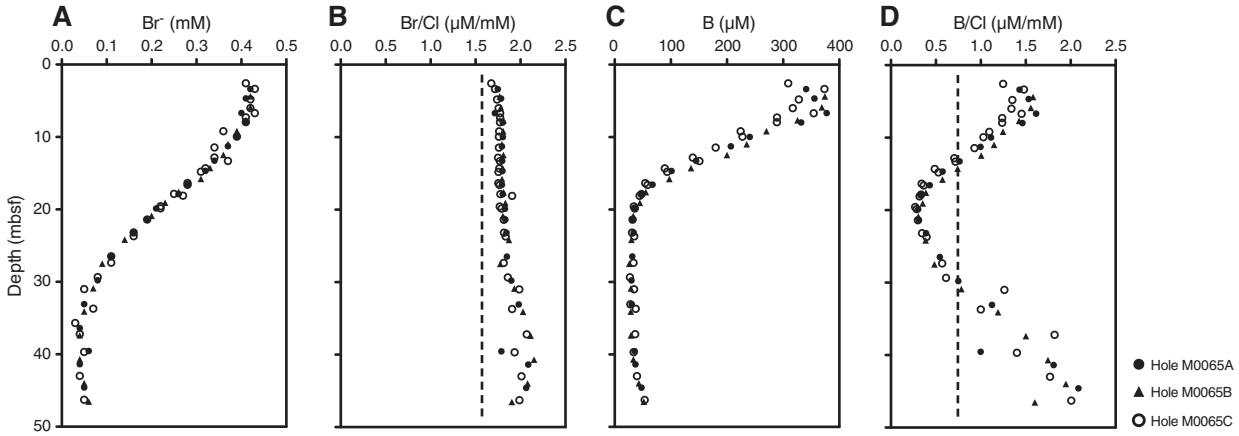

Figure F11. Concentrations and ratios of (**A**) sodium, (**B**) potassium, (**C**) magnesium, (**D**) calcium, (**E**) sodium/chloride, (**F**) potassium/chloride, (**G**) magnesium/chloride, and (**H**) calcium/chloride from interstitial water samples, Site M0065. Dashed lines = seawater ratio.

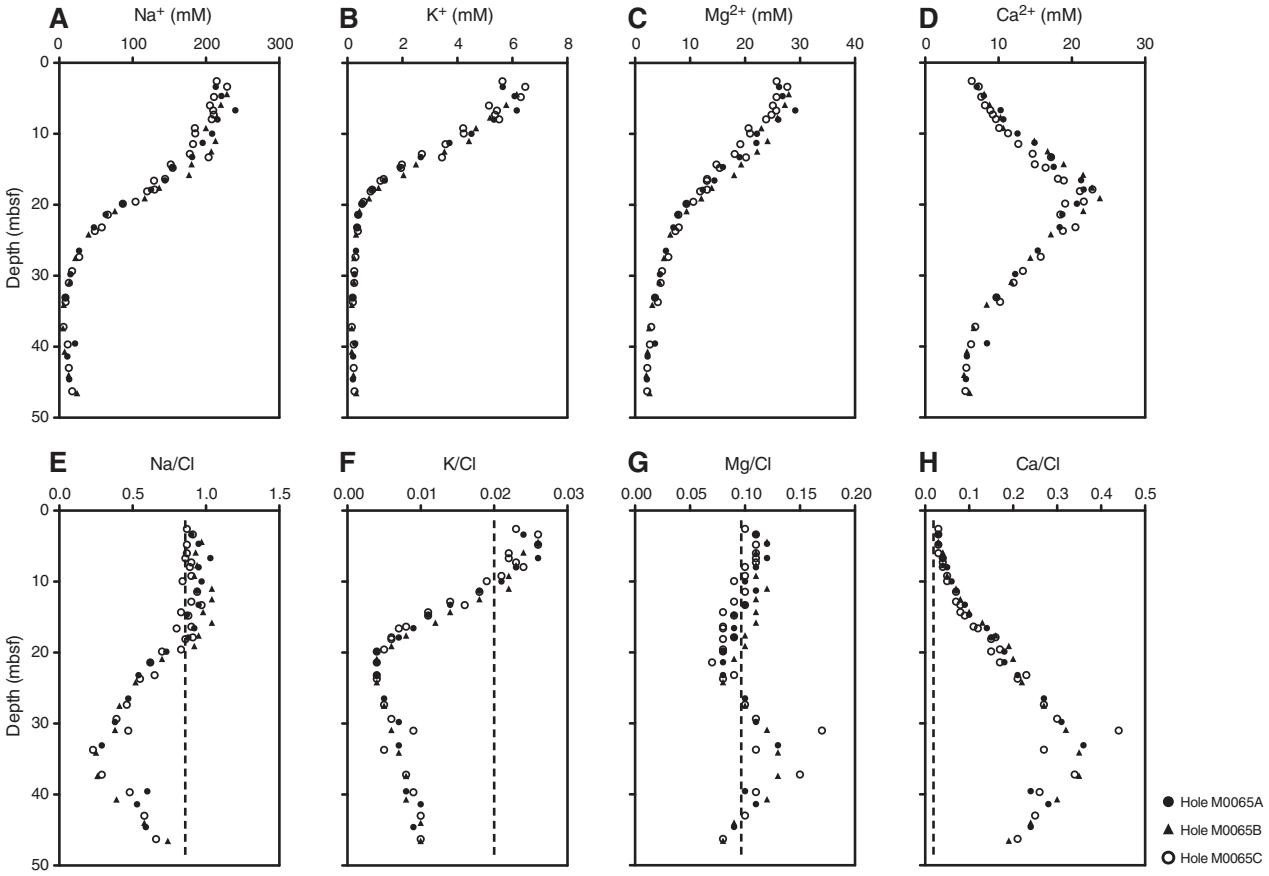

Figure F12. Concentrations of (**A**) dissolved silica, (**B**) lithium, (**C**) barium, and (**D**) strontium from interstitial water samples, Site M0065.

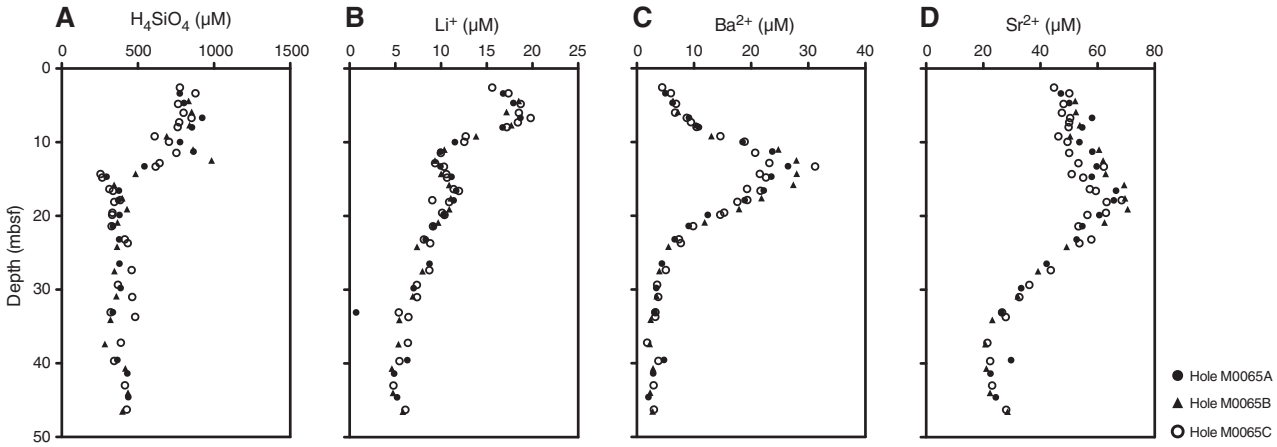

Figure F13. Sedimentary (**A**) total carbon (TC), (**B**) total organic carbon (TOC), (**C**) total inorganic carbon (TIC), and (**D**) total sulfur (TS) values, Site M0065.

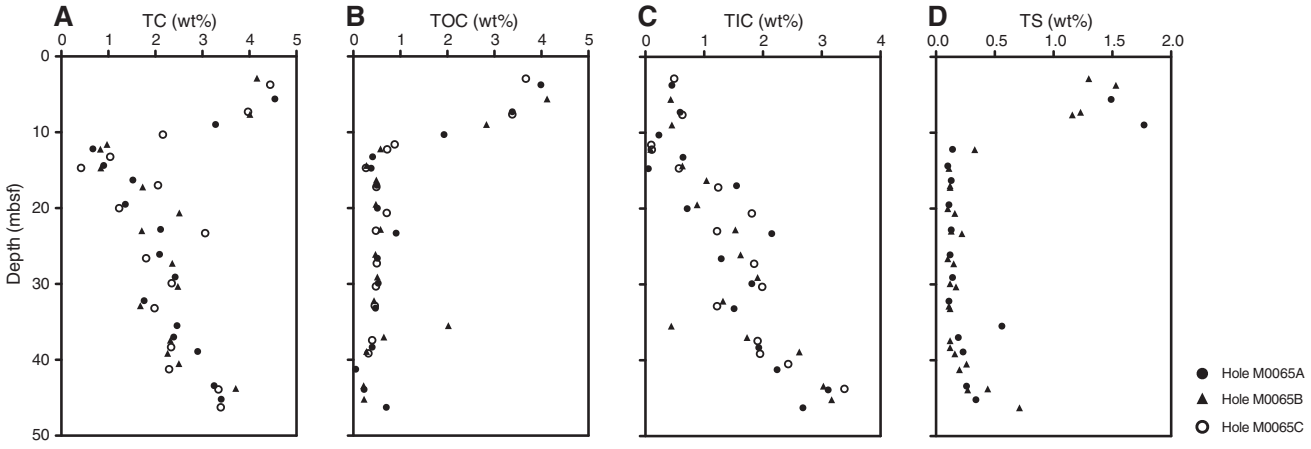

Figure F14. Natural gamma radiation (NGR) (cps), MSCL magnetic susceptibility (MS) (10^{-5} SI), MSCL non-contact resistivity (NCR) (Ωm), and color reflectance parameter a*, Hole M0065A.

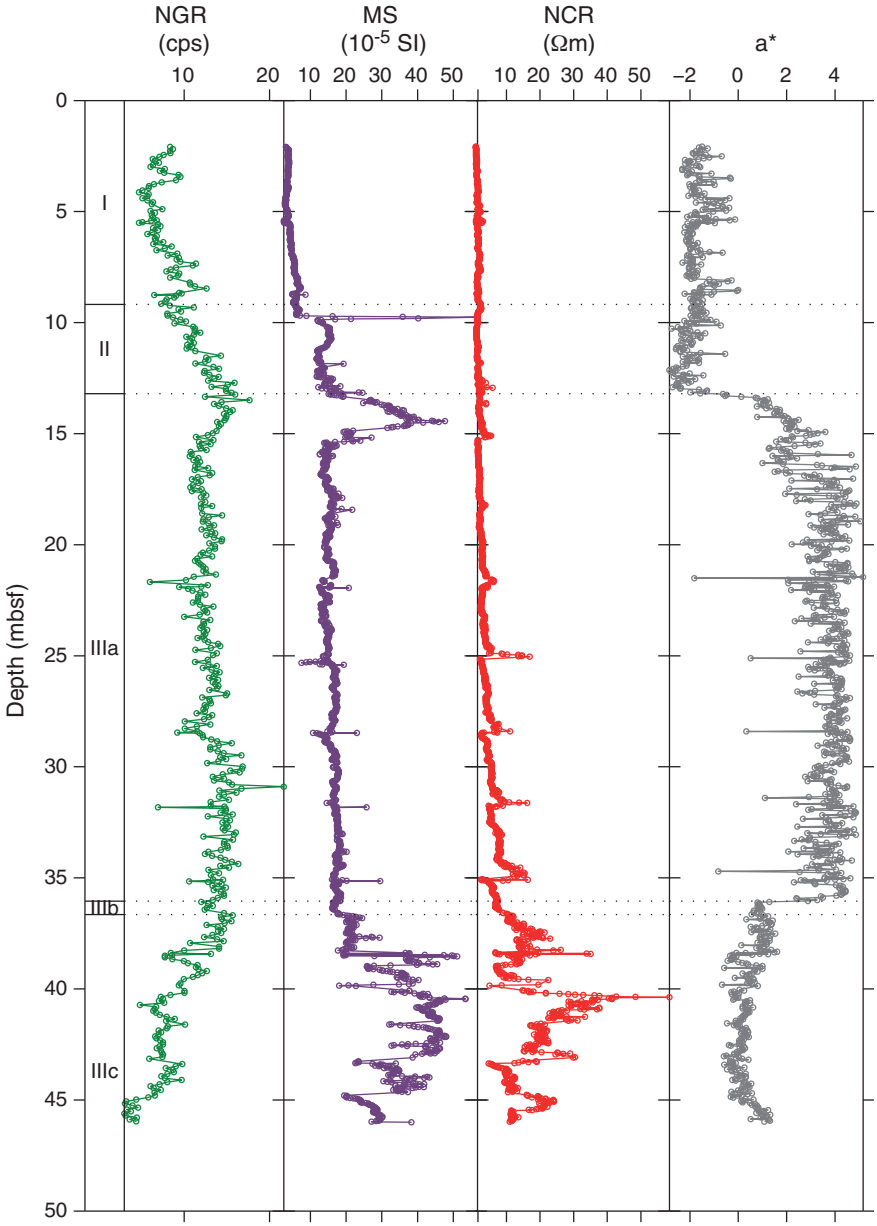

Figure F15. A. Gamma density (g/cm³) and discrete bulk density (g/cm³) measurements derived from pycnometer moisture and density analyses, Hole M0065A. **B.** MSCL *P*-wave and discrete velocity (m/s) measurements performed during the OSP, Hole M0065A.

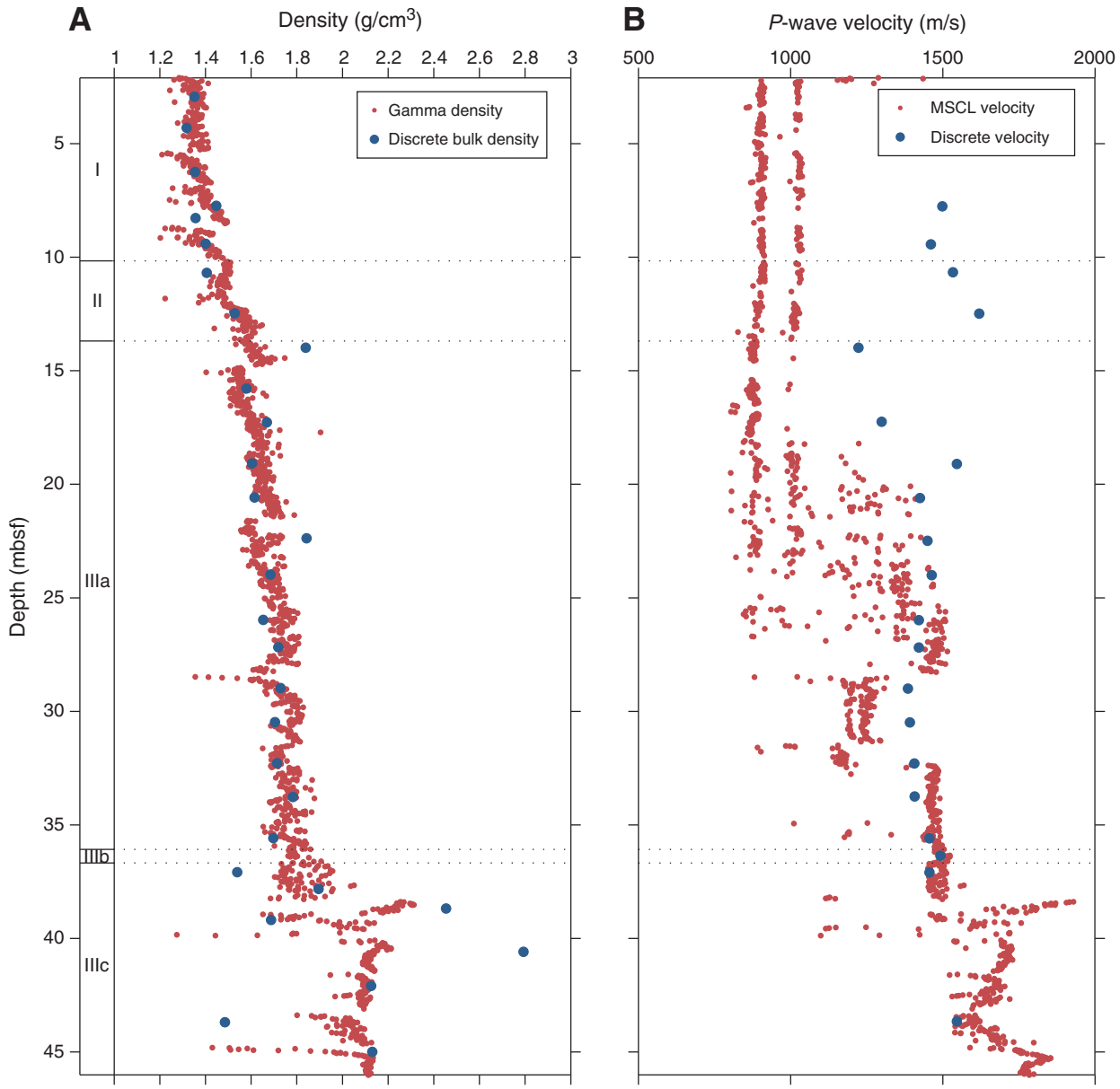

Figure F16. Correlation between gamma density (g/cm³) and discrete bulk density (g/cm³) measurements, Hole M0065A.

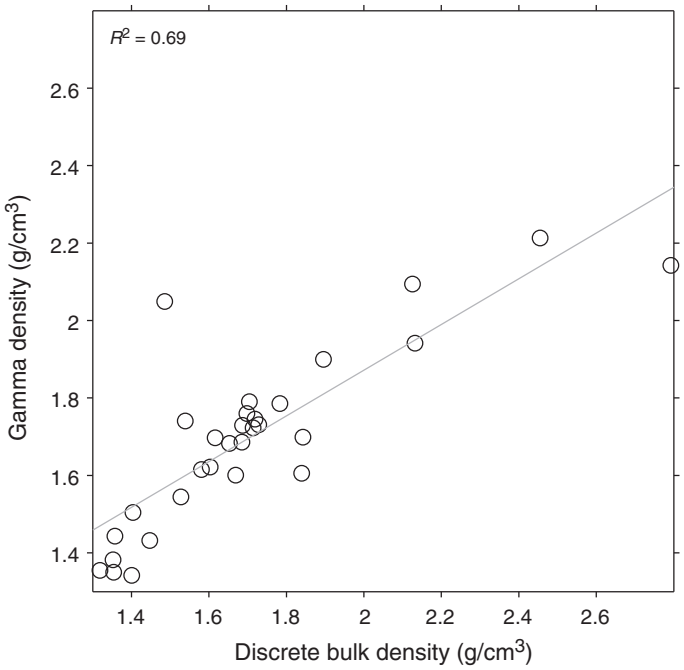

Figure F17. Plots and biplots of magnetic susceptibility (χ), natural remanent magnetization (NRM) intensity, and NRM inclination of discrete paleomagnetic samples, Holes M0065A and M0065C. Dashed line = geocentric axial dipole (GAD) prediction of inclination for the site latitude. AF = alternating field.

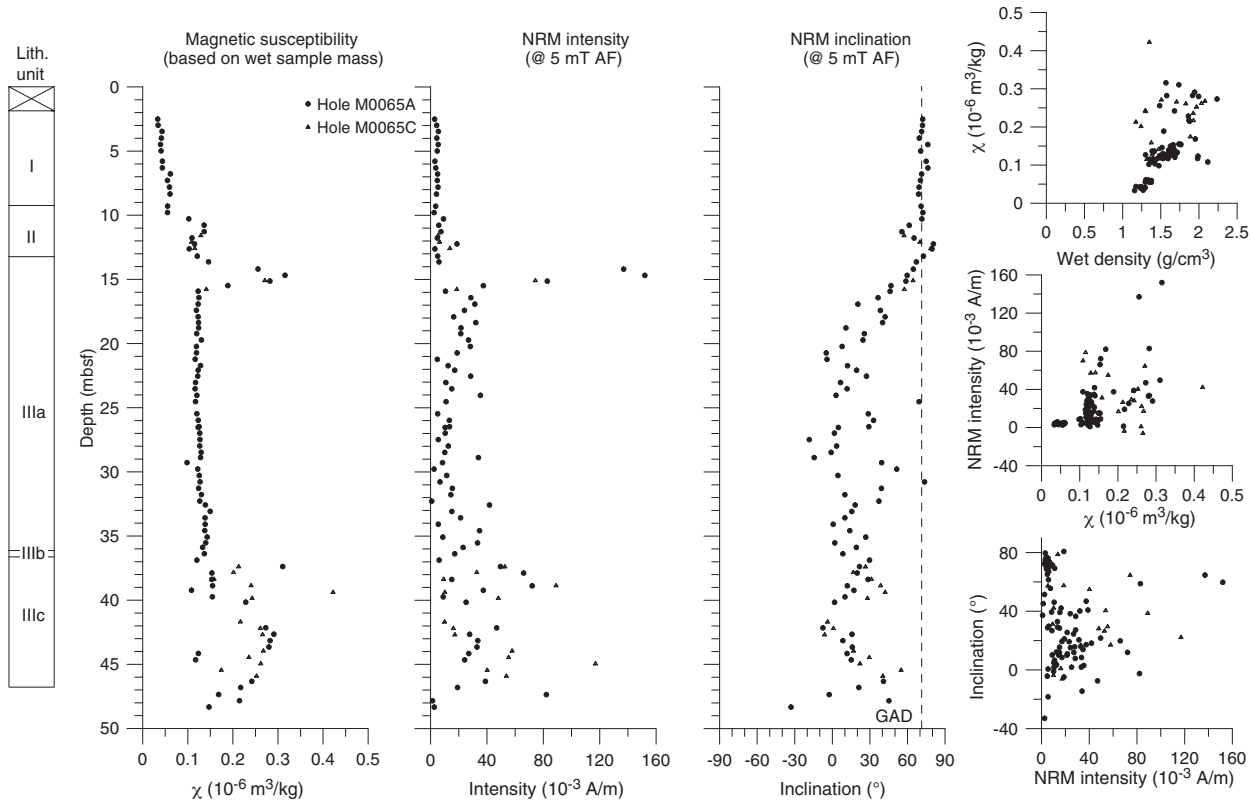

Figure F18. Plots of natural remanent magnetization (NRM) after alternating field (AF) demagnetization to 80 mT. **A.** Sample 347-M0065A-2H-2, 48 cm; 3.99 mbsf. **B.** Sample 347-M0065A-5H-2, 32 cm; 14.20 mbsf. **C.** Sample 347-M0065A-8H-1, 125 cm; 23.52 mbsf. **D.** Sample 347-M0065A-14H-2, 75 cm; 44.15 mbsf. Category 1 contains a very soft and shallow component, and the vector does not trend toward the origin. Category 2, 3, and 4 vectors trend toward the origin. More than 30% of the initial intensity of the Category 3 example remains after demagnetization at the 80 mT level. Open squares = vertical, solid squares = horizontal.

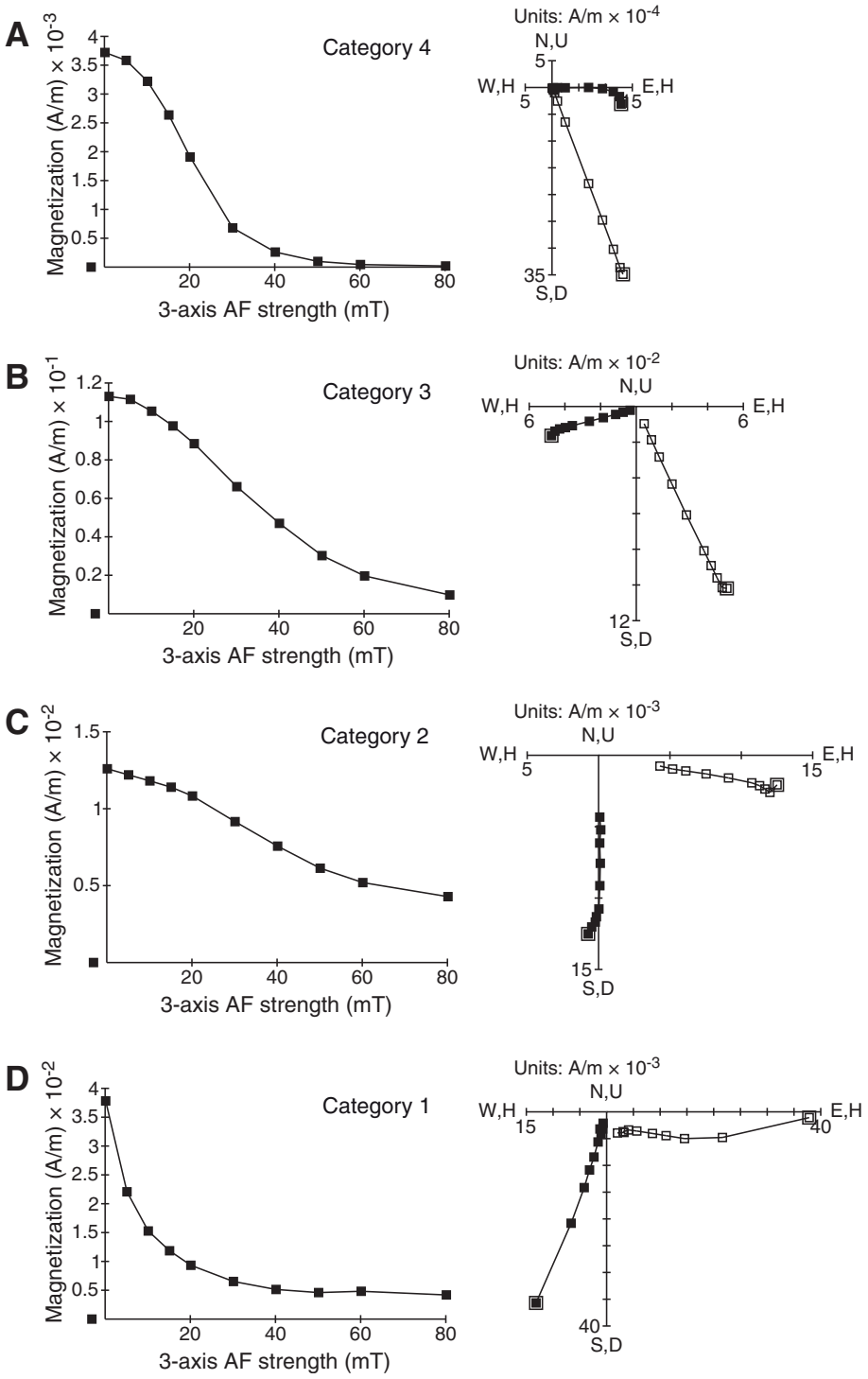

Figure F19. Plot of microbial cell abundances compared to chemical zonation and lithostratigraphy, Hole M0065C. **A.** Interstitial water alkalinity (blue dashed line) and salinity (red line). Green dashed line marks the boundary at ~12 mbsf; cell counting techniques produce similar results at deeper depths. **B.** Cell numbers obtained by flow cytometry (blue circles) and acridine orange direct count (red diamonds). Solid black line = global regression line of prokaryote cell numbers with depth, dashed lines = upper and lower 95% prediction limits for regression line (Roussel et al., 2008). Green dashed line marks the boundary at ~12 mbsf; cell counting techniques produce similar results at deeper depths. **C.** Lithology.

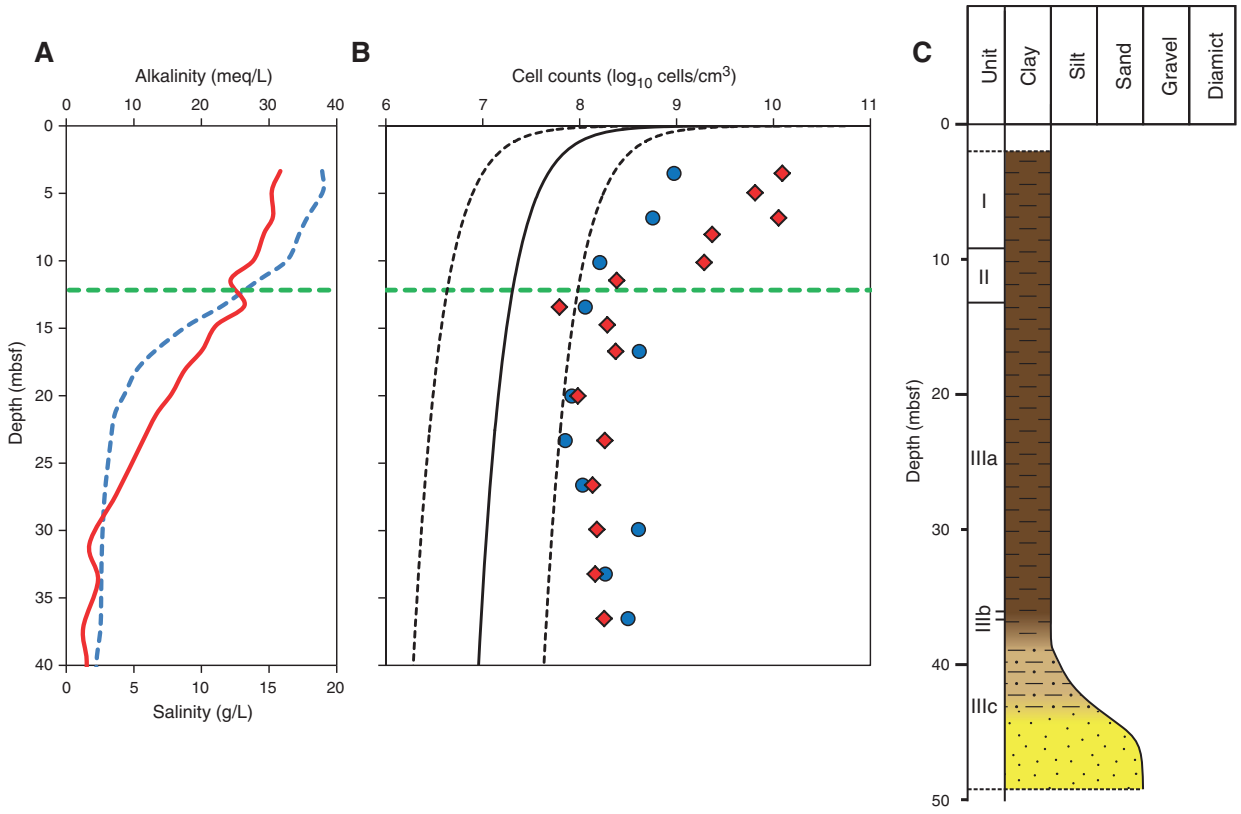

Figure F20. Comparison of paired counts between two methods of cell enumeration, Hole M0065C. Blue circles = results from deeper than 12 mbsf, green squares = results from shallower than 12 mbsf. Black dashed line = line of unity. FCM = flow cytometry, AODC = acridine orange direct count.

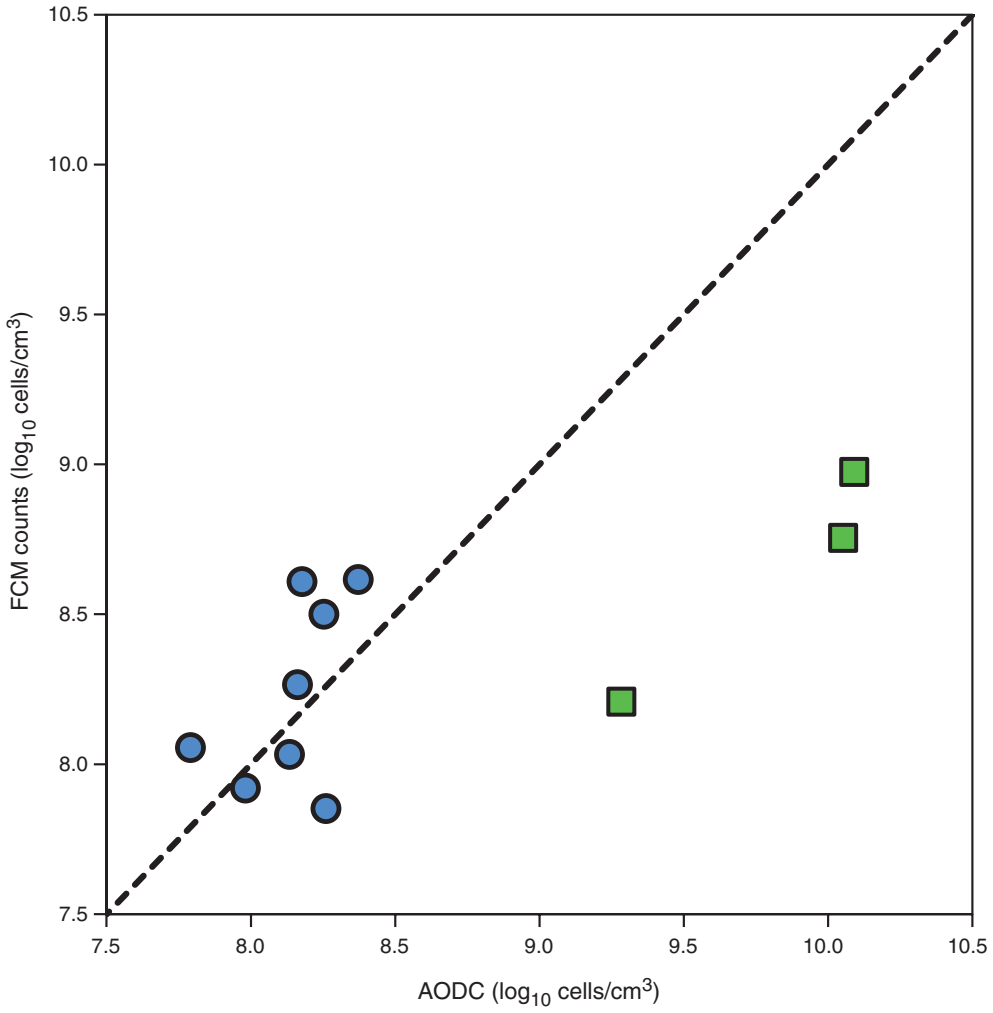

Figure F21. Plots of perfluorocarbon (PFC) tracer concentrations, Hole M0065C. **A.** Core liner fluid. **B.** Sediment core samples. (Continued on next page.)

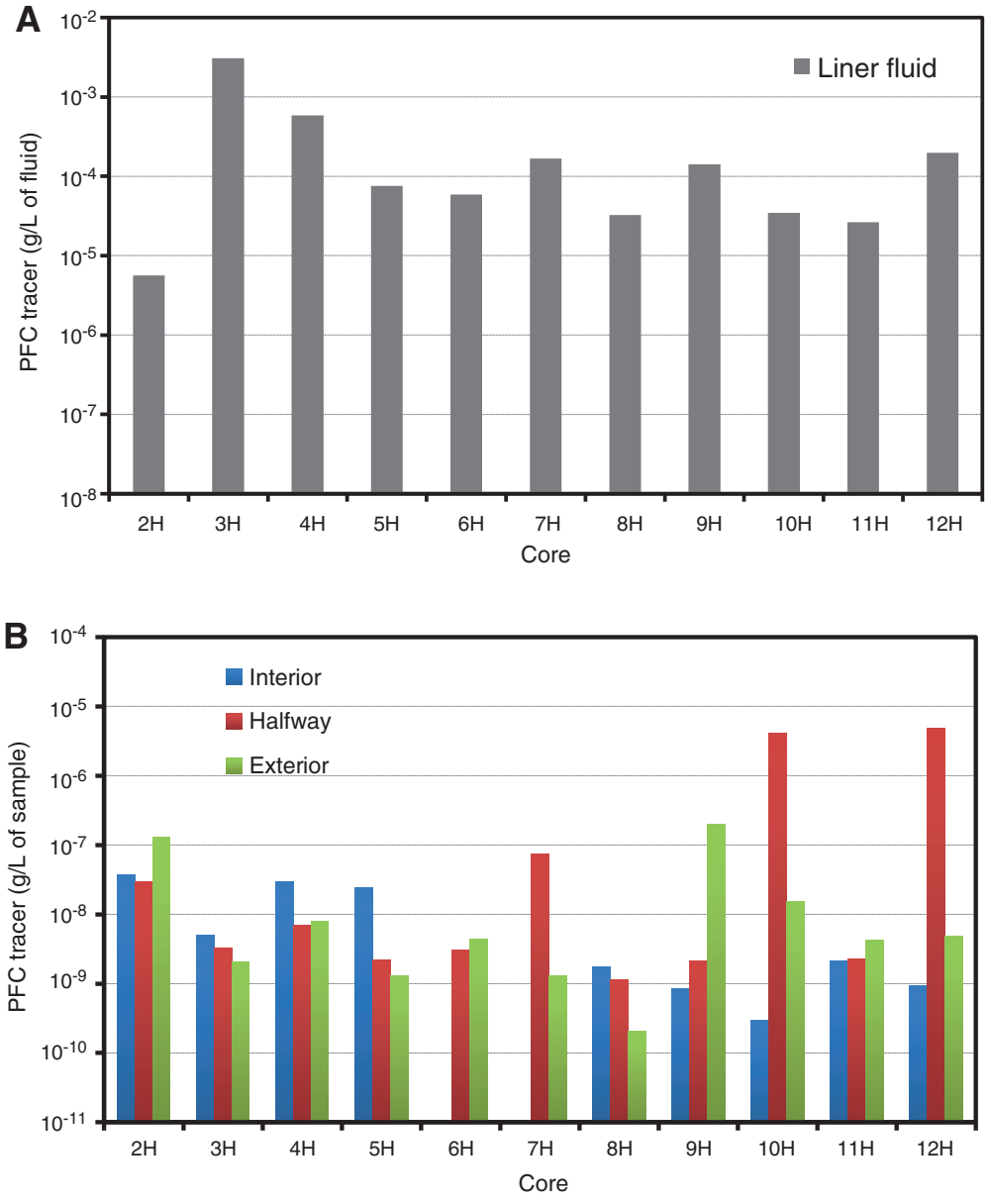

Figure F21 (continued). **C.** Estimated volume of liner fluid introduced into sediment cores shown as percentage of sediment core volume. **D.** Estimated potential number of contaminant cells per volume of sediment.

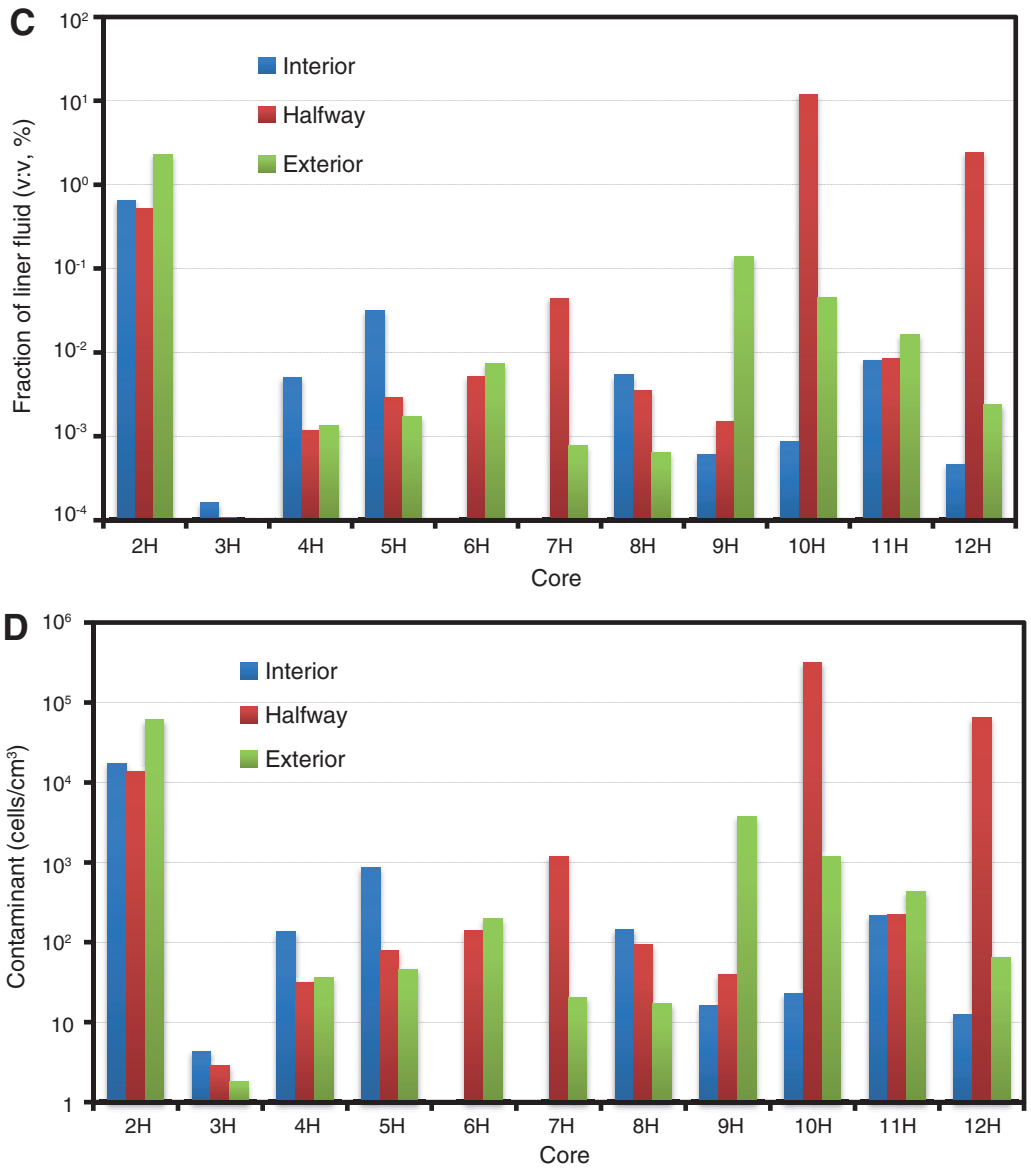

Figure F22. Plot of spliced magnetic susceptibility data, Hole M0065C.

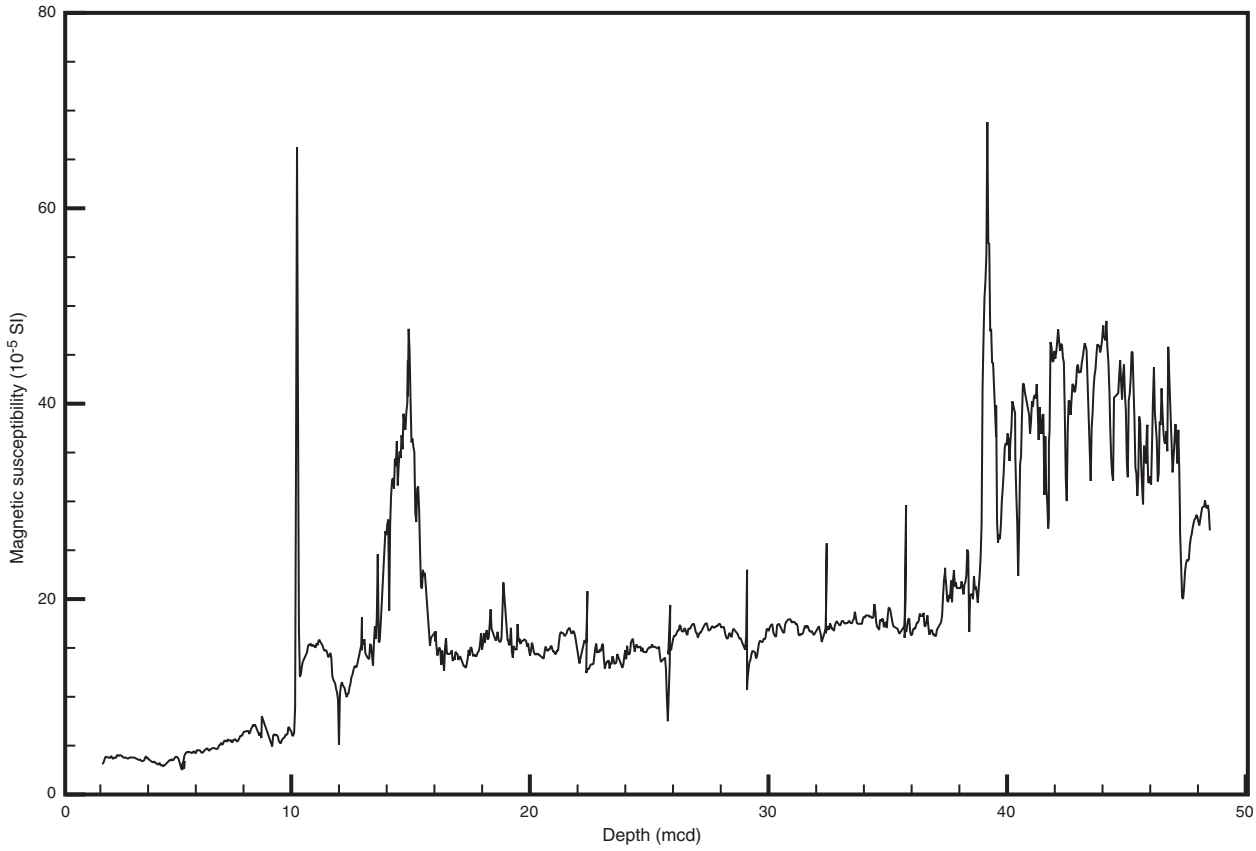

Figure F23. Comparison of smoothed downhole gamma ray and natural gamma ray measurements from core, Hole M0065A.

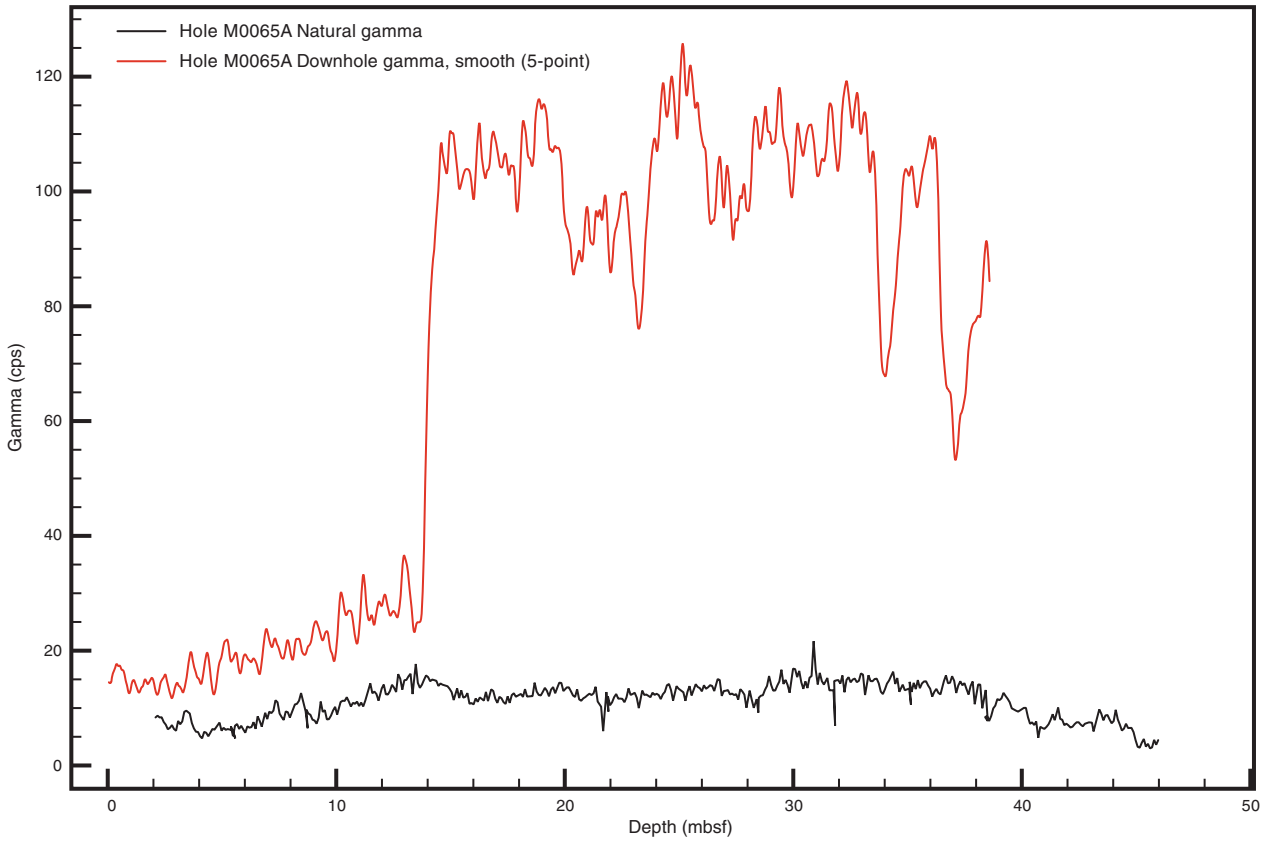

Figure F24. Correlation of seismic profile with lithostratigraphic boundaries and multisensor core logger magnetic susceptibility data, Site M0065. Precruise interpretation of seismic data is also shown: SF = seafloor, BH = Base Holocene, LG1 = Late Glacial 1 (HA), LG2 = Late Glacial II, BR = base depression.

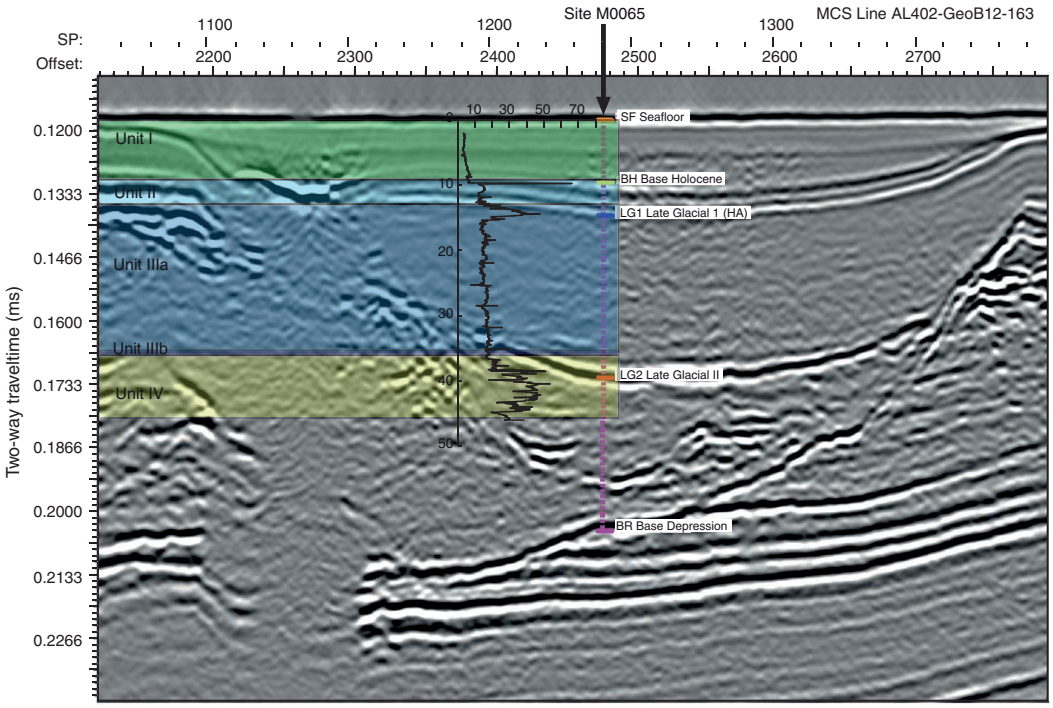

Figure F25. Gamma ray log and resistivity log, Hole M0065A. The drill pipe was set at 14 m WSF.

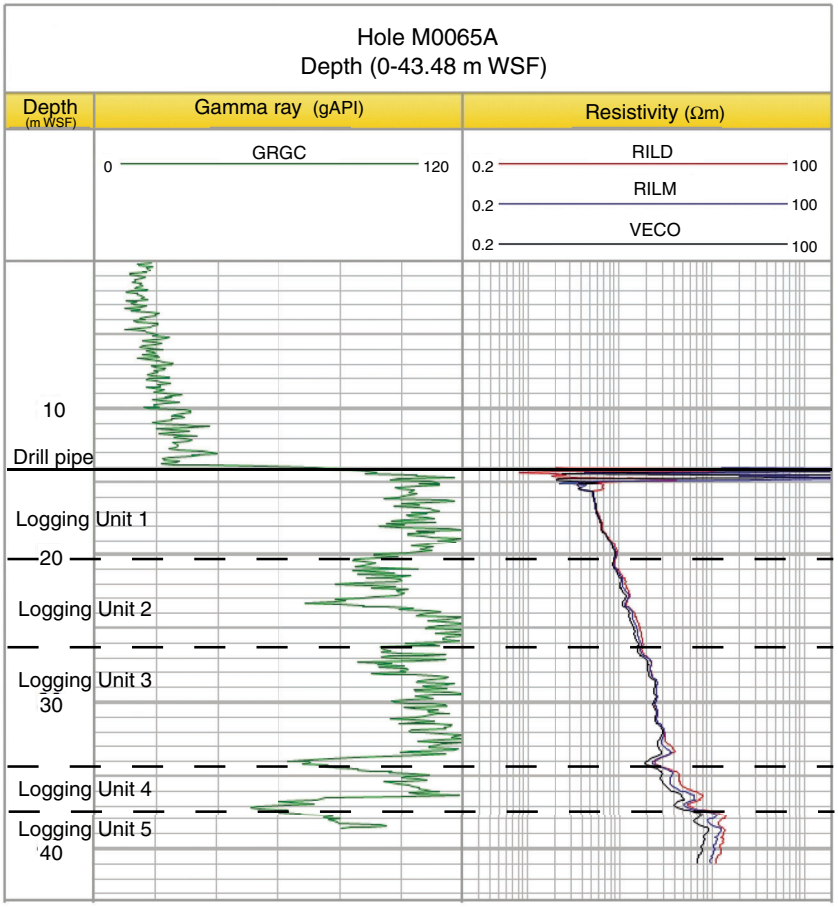

Figure F26. Gamma ray log, spectral gamma ray log, and sonic log, Hole M0065C. The drill pipe is set at 13.2 m WSF.

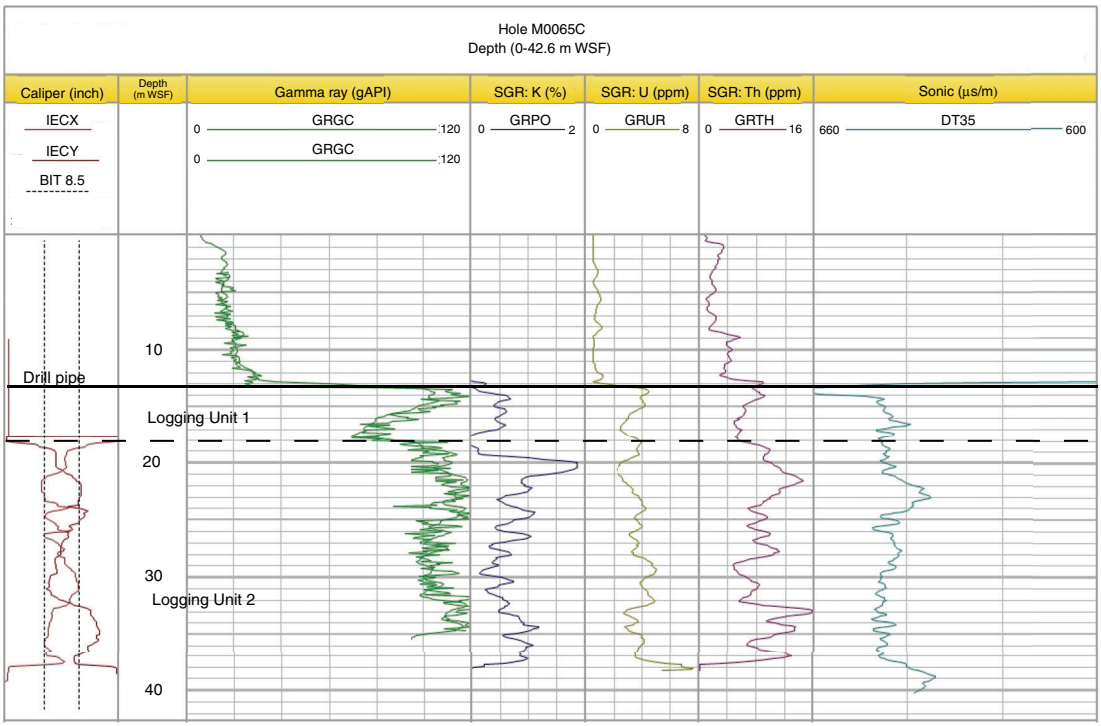

Table T1. Operations, Site M0065. (Continued on next two pages.)

Core	Coring method	Date (2013)	Time (UTC)	Depth (mbsf) Top	Depth (mbsf) Bottom	Recovered (m)	Recovery (%)	Mud type	Comments
347-M0065A-									
		23 Oct	1400						Arrived on site; built a differential GPS model
		23 Oct	1430						Lowered template into moonpool; checked bit and prepared for ROV survey
		23 Oct	1442						ROV in water and running down to seabed for predrilling survey
		23 Oct	1610						Derigged ROV and cleaned; prepared drill floor for operations
		23 Oct	1655						Lowered seabed template
		23 Oct	1715						Ran pipe
1O	NCA	23 Oct	1835	0.00	2.00	0.00	0	Seawater	Washed down through possible contaminants
2H	PCS	23 Oct	1850	2.00	5.30	3.61	109.39	Seawater	
3H	PCS	23 Oct	1920	5.30	8.60	3.52	106.67	Seawater	53 bar
4H	PCS	23 Oct	2000	8.60	11.90	3.52	106.67	Seawater	48 bar
5H	PCS	23 Oct	2035	11.90	15.20	3.67	111.21	Seawater	36 bar
6H	PCS	23 Oct	2115	15.20	18.50	3.52	106.67	Seawater	
7H	PCS	23 Oct	2212	18.50	21.80	3.53	106.97	Seawater	35 bar
8H	PCS	23 Oct	2240	21.80	25.10	3.68	111.52	Seawater	70 bar
9H	PCS	23 Oct	2325	25.10	28.40	3.43	103.94	Seawater	Did not appear to fire, even on second attempt, may have fired on the way down; collected a full sample
10H	PCS	24 Oct	0015	28.40	31.70	3.49	105.76	Seawater	55 bar
11H	PCS	24 Oct	0040	31.70	35.00	3.51	106.36	Seawater	65 bar
12H	PCS	24 Oct	0122	35.00	38.30	3.60	109.09	Seawater	50 bar
13H	PCS	24 Oct	0205	38.30	40.00	1.62	95.29	Seawater	110 bar and did not drop below 40 bar on release, hence not full stroke
14H	PCS	24 Oct	0255	40.00	43.30	3.45	104.55	Guar	70 bar
15H	PCS	24 Oct	0325	43.30	46.60	3.03	91.82	Guar	130 bar
16O	NCA	24 Oct	0507	46.60	49.60	0.00	0	Guar	Open hole to try and ascertain if in stones, only sand and clay evident
17S	HS	24 Oct	0720	49.60	49.70	0.10	100		Hammer sample 25 blows showed dense fine sand in hole
18O	NCA	24 Oct	0730	49.70	52.60	0.00	0	Guar	Open hole to next hammer sample interval
19S	HS	24 Oct	0838	52.60	52.65	0.05	100		Fine sand in hammer sample
20O	NCA	24 Oct	0904	52.65	55.60	0.00	0	Guar	
21S	HS	24 Oct	1000	55.60	55.70	0.10	100		
22O	NCA	24 Oct	1020	55.70	58.60	0.00	0	Guar	
23S	HS	24 Oct	1050	58.60	58.75	0.15	100		
24O	NCA	24 Oct	1115	58.75	59.60	0.00	0	Guar	
25S	HS	24 Oct	1140	59.60	59.70	0.10	100		
26O	NCA	24 Oct	1150	59.70	60.60	0.00	0	Guar	
27S	HS	24 Oct	1205	60.60	60.70	0.10	100		
28O	NCA	24 Oct	1225	60.70	61.60	0.00	0	Guar	
29S	HS	24 Oct	1215	61.60	61.70	0.10	100		
30O	NCA	24 Oct	1300	61.70	63.60	0.00	0	Guar	
31S	HS	24 Oct	1320	63.60	63.65	0.05	100		
		24 Oct	1345						Powerpack pressure release valve problem required shutdown
32O	NCA	24 Oct	1410	63.65	65.60	0.00	0	Guar	
33S	HS	24 Oct	1440	65.60	65.75	0.15	100		
34O	NCA	24 Oct	1455	65.75	67.60	0.00	0	Guar	
35S	HS	24 Oct	1520	67.60	67.75	0.15	100		
36O	NCA	24 Oct	1535	67.75	69.60	0.00	0	Guar	
37S	HS	24 Oct	1600	69.60	69.65	0.05	100		
38O	NCA	24 Oct	1615	69.65	71.60	0.00	0	Guar	
39S	HS	24 Oct	1635	71.60	71.62	0.02	100		
40O	NCA	24 Oct	1654	71.62	73.60	0.00	0	Guar	
41S	HS	24 Oct	1714	73.60	73.60	0.00	0		Slight show of chalk on inside of shoe; reran insert bit for short run and rehammer
42O	NCA	24 Oct	1720	73.60	73.80	0.00	0	Guar	Low flush rate to retain as much disturbed material as possible at the bottom for the hammer to collect

Table T1 (continued). (Continued on next page.)

Core	Coring method	Date (2013)	Time (UTC)	Depth (mbsf) Top	Depth (mbsf) Bottom	Recovered (m)	Recovery (%)	Mud type	Comments
43S	HS	24 Oct	1730	73.80	73.90	0.10	100		50 blows; bedrock in shoe
		24 Oct	1745						End of hole
		24 Oct	1750					Guar	Mud flush before pulling back to 3.4 mbsf for logging; changed to 12 m below seabed at drillers request
		24 Oct	1830						Set up logging tools
		24 Oct	1900						First logging run to 41.5 mbsf
		24 Oct	1940						Second logging run: hole collapsed at bottom of pipe; dismantled logging deck
		24 Oct	2030						Discussed possibility of wiper trip with Logging Staff Scientist and Co-Chief and agreed to attempt for second run; wiper trip for 3 pipes to clear hole for second logging run
		24 Oct	2110						Rerigged logging deck; 35 kt wind and building
		24 Oct	2120						Attempted second logging run, only achieved 5 m open hole
		24 Oct	2130						Recovered tools and dismantled logging deck
		24 Oct	2145						Tripped pipe
347-M0065B-									
		24 Oct	2230						On site; lowered seabed frame and added drill pipe
1O	NCA	24 Oct	2310	0.00	3.00	0.00	0	Seawater	Open hole first section to avoid possible contamination
2H	PCS	24 Oct	2314	3.00	6.30	3.62	109.7	Seawater	
3H	PCS	25 Oct	0005	6.30	9.60	3.66	110.91	Seawater	
4H	PCS	25 Oct	0048	9.60	12.90	3.37	102.12	Seawater	Core degassing a lot
5H	PCS	25 Oct	0126	12.90	16.20	3.53	106.97	Seawater	
6H	PCS	25 Oct	0210	16.20	19.50	3.45	104.55	Seawater	45 bar
7H	PCS	25 Oct	0258	19.50	22.80	3.59	108.79	Seawater	
8H	PCS	25 Oct	0338	22.80	26.10	3.54	107.27	Seawater	
9H	PCS	25 Oct	0440	26.10	29.40	3.43	103.94	Seawater	
10H	PCS	25 Oct	0455	29.40	32.70	3.51	106.36	Seawater	
11H	PCS	25 Oct	0600	32.70	36.00	3.50	106.06	Seawater	
12H	PCS	25 Oct	0635	36.00	39.30	3.41	103.33	Seawater	
13H	PCS	25 Oct	0705	39.30	42.60	3.14	95.15	Seawater	
14H	PCS	25 Oct	0740	42.60	45.90	3.35	101.52	Seawater	
15H	PCS	25 Oct	0820	45.90	46.90	0.84	84	Seawater	
16O	NCA	25 Oct	0855	46.90	48.90	0.00	0	Seawater	
17S	HS	25 Oct	0920	48.90	49.20	0.30	100		Sand with smearing of clay/silt
18S	HS	25 Oct	1000	49.20	49.30	0.10	100		
		25 Oct	1015						End of hole
		25 Oct	1015						Tripped pipe above seabed to allow bumping over to Hole M0065C
347-M0065C-									
		25 Oct	1110						On site; lowered seabed frame and added drill pipe
1O	NCA	25 Oct	1115	0.00	2.00	0.00	0	Seawater	Open hole first section to avoid possible contamination
2H	PCS	25 Oct	1125	2.00	5.30	3.75	113.64	Seawater	
3H	PCS	25 Oct	1205	5.50	8.60	3.60	116.13	Seawater	
4H	PCS	25 Oct	1330	8.60	11.90	3.64	110.3	Seawater	
5H	PCS	25 Oct	1420	11.90	15.20	3.68	111.52	Seawater	
6H	PCS	25 Oct	1509	15.20	18.50	3.50	106.06	Seawater	
7H	PCS	25 Oct	1636	18.50	21.80	3.44	104.24	Seawater	64 bar
8H	PCS	25 Oct	1730	21.80	25.10	3.54	107.27	Seawater	
9H	PCS	25 Oct	1823	25.10	28.40	3.39	102.73	Seawater	65 bar
10H	PCS	25 Oct	1921	28.40	31.70	3.36	101.82	Seawater	61 bar, no lower shoe sample
11H	PCS	25 Oct	2015	31.70	35.00	3.60	109.09	Seawater	62 bar
12H	PCS	25 Oct	2110	35.00	38.30	3.67	111.21	Seawater	
13H	PCS	25 Oct	2205	38.30	41.60	3.25	98.48	Seawater	60 bar
14H	PCS	25 Oct	2308	41.60	44.90	3.30	100	GS550	70 bar

Table T1 (continued).

Core	Coring method	Date (2013)	Time (UTC)	Depth (mbsf) Top	Depth (mbsf) Bottom	Recovered (m)	Recovery (%)	Mud type	Comments
15H	PCS	25 Oct	2340	44.90	47.90	2.87	95.67	GS550	150 bar and pressure stayed full until driller lifted the string
		26 Oct	0015						Drilling ended; prepared for logging
		26 Oct	0020						Filled hole with very heavy mud
		26 Oct	0040						Lifted drill string to 14 mbsf
		26 Oct	0120						Logging run started; reached 40 mbsf
		26 Oct	0220						Second logging string in the hole
		26 Oct	0310						Started lifting drill string with personnel in full PPE hosing potentially contaminated pipes down with water

HS = hammer sampler, NCA = noncoring assembly, PCS = piston coring system. ROV = remotely operated vehicle, PPE = personal protective equipment.

Table T2. Diatom species, Site M0065.

Taxonomic list
Marine taxa
Actinoptychus senarius (Ehrenberg) Ehrenberg
Dimeregramma minor (Gregory) Ralfs
Diploneis decipiens var. *parallela* A. Cleve
Hyalodiscus scoticus (Kützing) Grunow
Lyrella cf. *spectabilis* (Gregory) D.G. Mann
Opephora marina (Gregory) Petit
Opephora minuta (Cleve-Euler) Witkowski
Pseudosolenia calcar-avis (Schultze) B.G. Sundström
Thalassiosira eccentrica (Ehrenberg) Cleve
Thalassiosira oestrupii (Ostenfeld) Hasle
Toxarium undulatum Bailey
Brackish-marine taxa
Chaetoceros resting spores spp.
Cocconeis speciosa Gregory
Fallacia pseudony (Hustedt) D.G. Mann
Grammatophora oceanica Ehrenberg
Rhabdonema arcuatum (Lyngbye) Kützing
Rhabdonema minutum Kützing
Thalassionema nitzschioides (Grunow) Mereschkowsky
Brackish taxa
Achnanthes lemmermannii Hustedt
Amphora robusta Gregory
Brachysira aponina Kützing
Chamaepinnularia witkowskii (Lange-Bertalot and Metzeltin) Kulikovskiy and Lange-Bertalot
Cocconeis scutellum Ehrenberg
Cyclotella choctawhatcheeana Prasad
Diploneis didyma (Ehrenberg) Ehrenberg
Diploneis interrupta (Kützing) Cleve
Diploneis stroemii Hustedt
Epithemia adnata (Kützing) Brébisson
Fragilaria gedanensis Witkowski
Martyana schulzii (Brockmann) Snoeijs
Mastogloia pusilla Grunow
Navicula palpebralis Brébisson ex W. Smith
Navicula peregrina (Ehrenberg) Kützing
Paralia sulcata (Ehrenberg) Cleve
Planothidium quarnerensis (Grunow) Witkowski, Lange-Bertalot and Metzelin
Rhoicosphenia curvata (Kützing) Grunow
Thalassiosira proschkinae Makarova
Brackish-freshwater taxa
Actinocyclus octonarius var. *crassus* (W. Smith) Hendey
Amphora pediculus (Kützing) Grunow ex A. Schmidt
Aneumastus minor (Hustedt) Lange-Bertalot
Cymatopleura elliptica (Brébisson) W. Smith
Diploneis domblittensis (Grunow) Cleve
Diploneis smithii (Brébisson) Cleve
Epithemia turgida var. *westermannii* (Ehrenberg) Grunow
Fragilariopsis cylindrus (Grunow) Krieger
Gyrosigma acuminatum (Kützing) Rabenhorst
Melosira lineata (Dillwyn) Agardh
Navicula capitata var. *hungarica* (Grunow) R. Ross
Pseudostaurosira brevistriata (Grunow) Williams and Round
Thalassiosira baltica (Grunow) Ostenfeld
Freshwater taxa
Aneumastus tusculus (Ehrenberg) D.G. Mann and A.J. Stickle
Aulacoseira ambigua (Grunow) Simonsen
Aulacoseira subarctica (O. Müller) Haworth
Aulacoseira islandica (O. Müller) Simonsen
Cocconeis disculus (Schumann) Cleve
Cocconeis neodiminuta Krammer
Cocconeis pseudothumensis Reichard
Cyclotella rossii Håkansson
Cyclotella schumannii (Grunow) Håkansson
Encyonema minutum (Hilse) D.G. Mann
Fragilaria heidenii Østrup
Martyana martyii (Héribaud-Joseph) Round
Navicula jentzschii Grunow
Sellaphora pupula (Kützing) Mereschowsky
Staurosira venter (Ehrenberg) H. Kobayasi
Stephanodiscus cf. *alpinus* Hustedt
Stephanodiscus medius Håkansson
Stephanodiscus neoastraea Håkansson and Hickel
Stephanodiscus spp.
Tabellaria flocculosa (Roth) Kützing

Salinity affinities follows Snoeijs et al. (1993–1998). Diatom authorities according to AlgaeBase (www.algaebase.org).

Table T3. Diatoms, Hole M0065A. This table is available in **oversized format**.

Table T4. Foraminifers, Site M0065.

Hole, core, section, interval (cm)	Depth (mbsf) Top	Depth (mbsf) Bottom	Abundance	Number of species	*Elphidium albiumbilicatum*	*Elphidium excavatum clavatum*	*Elphidium excavatum selseyensis*	*Elphidium incertum*	*Elphidium williamsoni*	Other *Elphidium* and *Haynesina* spp.
347-										
M0065A-2H-1, 15–17	2.15	2.17	R	2		x	x			
M0065A-2H-1, 75–77	2.75	2.77	V	2		x				x
M0065B-2H-1, 15–17	3.15	3.17	C	4	x	x	x	x		
M0065B-2H-1, 76–78	3.76	3.78	C	4		x	x		x	x
M0065B-2H-2, 15–17	4.65	4.67	A	4		x	x		x	x
M0065A-2H-CC	5.59	5.61	C	2		x	x			
M0065C-2H-CC	5.73	5.75	F	2		x				x
M0065B-2H-CC	6.60	6.62	C	3		x	x			x
M0065A-3H-2, 15–17	6.95	6.97	F	2	x	x				
M0065B-3H-2, 15–17	7.95	7.97	R	3		x	x		x	
M0065A-3H-CC	8.81	8.82	R	1		x				
M0065C-3H-CC	8.88	8.90	V	1		x				
M0065B-3H-CC	9.92	9.96	B							
M0065A-4H-2, 15–17	10.25	10.27	B							
M0065B-4H-2, 15–17	11.25	11.27	B							
M0065A-4H-CC	11.90	12.12	V	1		x				
M0065C-4H-CC	12.20	12.24	B							
M0065B-4H-CC	12.80	12.97	B							
M0065A-5H-CC	15.24	15.57	B							
M0065B-5H-CC	16.40	16.43	B							
M0065A-6H-2, 15–17	16.84	16.86	B							
M0065A-6H-CC	18.46	18.72	B							
M0065B-6H-CC	19.60	19.65	B							
M0065A-7H-CC	22.00	22.03	B							
M0065B-7H-CC	23.07	23.09	B							
M0065A-8H-2, 15–17	23.45	23.47	B							
M0065A-8H-CC	25.45	25.48	B							
M0065B-8H-CC	26.32	26.34	B							
M0065A-10H-2, 15–17	30.05	30.07	B							
M0065A-10H-CC	31.86	31.89	B							
M0065B-10H-CC	32.89	32.91	B							
M0065A-11H-CC	35.19	35.21	B							
M0065B-11H-CC	36.19	36.20	B							
M0065A-12H-1, 122–124	36.22	36.24	B							
M0065A-12H-2, 3–5	36.53	36.55	B							
M0065A-12H-3, 15–17	38.15	38.17	B							
M0065A-12H-CC	38.56	38.60	B							
M0065A-14H-2, 15–17	41.65	41.67	B							
M0065B-13H-CC	42.43	42.44	B							
M0065A-14H-CC	43.45	43.50	B							
M0065B-14H-CC	45.75	45.90	B							
M0065B-15H-1, 20–22	46.10	46.12	B							
M0065A-15H-CC	46.29	46.31	B							
M0065B-15H-1, 41–43	46.31	46.33	B							
M0065B-15H-1, 43–45	46.33	46.35	B							
M0065B-17S-CC	49.17	49.20	B							
M0065A-17H-CC	49.64	49.70	B							
M0065A-25S-CC	59.64	59.70	B							
M0065A-27S-CC	60.64	60.70	B							
M0065A-29S-CC	61.65	61.70	B							
M0065A-33S-CC	65.64	65.75	B							
M0065A-35S-CC	67.65	67.75	B							
M0065A-37S-CC	69.63	69.65	B							
M0065A-39S-CC	71.60	71.62	B							
M0065A-43S-CC	73.85	73.90	B							

Abundance: A = abundant, C = common, F = few, R = rare, B = barren, V = very high.

Table T5. Distribution and abundance of ostracods, Site M0065.

Core, section, interval (cm)	Depth (mbsf)	Overall abundance/20 cm^3	Abundance (offshore samples, 5–30 cm^3)	*Cytheropteron latissimum*	*Robertsonites tuberculatus*	*Palmoconcha* spp.	*Paracyprideis* sp.	*Sarsicytheridea bradii*	Undetermined
347-M0065A-									
2H-1, 15–17	2.16	R		R				R	
2H-1, 75–77	2.76	B							
2H-CC, 28–30	5.59		B						
3H-2, 15–17	6.96	R				R			
3H-CC, 24–25	8.81		F			F			
4H-2, 15–17	10.26	B							
4H-CC, 0–22	11.90		B						
5H-CC, 0–33	15.24		B						
6H-2, 15–17	16.85	B							
6H-CC, 0–26	18.46		B						
7H-CC, 27–30	22.00		B						
8H-2, 15–17	23.46	B							
8H-CC, 34–37	25.45		B						
10H-2, 15–17	30.06	B							
10H-CC, 17–20	31.86		B						
11H-CC, 20–22	35.19		B						
12H-1, 122–124	36.23	B							
12H-2, 3–5	36.54	B							
12H-3, 15–17	38.16	B							
12H-CC, 23–27	38.56		B						
14H-2, 15–17	41.66	B							
14H-CC, 28–33	43.45		B						
15H-CC, 24–26	46.29		B						
17H-CC, 4–10	49.64		B						
25S-CC, 4–10	59.64		B						
27S-CC, 4–10	60.64		B						
29S-CC, 5–10	61.65		B						
33S-CC, 4–15	65.64		B						
35S-CC, 5–15	67.65		B						
37S-CC, 2–5	69.62		B						
39S-CC, 0–2	71.60		B						
43S-CC, 5–10	73.85		B						
347-M0065B-									
2H-1, 15–17	3.16	R			R		R		R
2H-1, 76–78	3.77	B							
2H-2, 15–17	4.66	B							
2H-CC, 21–23	6.60		R			R			
3H-2, 15–17	7.96		C		R	C			
3H-CC, 24–27	9.93		B						
4H-2, 15–17	11.26	B							
4H-CC, 13–17	12.93		B						
5H-CC, 25–28	16.40		B						
6H-CC, 16–21	19.60		B						
7H-CC, 28–30	23.07		B						
8H-CC, 22–24	26.32		B						
10H-CC, 23–25	32.89		B						
11H-CC, 29–30	36.19		B						
13H-CC, 4–5	42.43		B						
14H-CC, 0–15	45.75		B						
17S-CC, 27–30	49.17		B						
347-M0065C-									
2H-CC, 25–27	5.73		R			R			
3H-CC, 28–30	8.88		F			F			
4H-CC, 30–34	12.20		B						

Abundance: C = common, F = few, R = rare, B = barren.

Table T6. Interstitial water geochemistry, Site M0065. This table is available in **oversized format**.

Table T7. Calculated salinity and elemental ratios of interstitial waters, Site M0065. (Continued on next page.)

Core, section, interval (cm)	Type	Depth (mbsf)	Cl^- based salinity	Na/Cl (mM/mM)	Ca/Cl (mM/mM)	Mg/Cl (mM/mM)	K/Cl (mM/mM)	Br/Cl (µM/mM)	B/Cl (µM/mM)
347-M0065A-									
2H-1, 135–140	Rh	3.38	14.94	0.90	0.03	0.11	0.02	1.75	1.43
2H-2, 115–120	Rh	4.68	14.56	0.95	0.03	0.12	0.03	1.78	1.53
3H-1, 135–140	Rh	6.68	14.65	1.03	0.04	0.12	0.03	1.71	1.62
3H-2, 115–120	Rh	7.98	14.24	0.95	0.05	0.11	0.02	1.80	1.46
4H-1, 135–140	Rh	9.98	13.54	0.97	0.06	0.10	0.02	1.80	1.11
4H-2, 115–120	Rh	11.28	13.03	0.94	0.07	0.11	0.02	1.79	1.00
5H-1, 135–140	Rh	13.28	11.92	0.95	0.09	0.10	0.01	1.80	0.76
5H-2, 124–129	Rh	14.67	11.08	0.87	0.10	0.09	0.01	1.80	0.57
6H-1, 134–139	Rh	16.57	9.78	0.92	0.14	0.09	0.01	1.79	0.43
6H-2, 135–120	Rh	17.87	8.89	0.88	0.15	0.09	0.01	1.80	0.34
7H-1, 135–140	Rh	19.88	7.35	0.73	0.18	0.08	0.00	1.83	0.30
7H-2, 135–140	Rh	21.38	6.35	0.62	0.18	0.08	0.00	1.83	0.31
8H-1, 135–140	Rh	23.18	5.43	0.54	0.21	0.08	0.00	1.84	0.39
9H-1, 135–140	Rh	26.48	3.60	0.47	0.27	0.10	0.01	1.85	0.54
10H-1, 135–140	Rh	29.78	2.49	0.38	0.31	0.11	0.01	1.90	0.75
11H-1, 135–140	Rh	33.08	1.69	0.29	0.36	0.13	0.01	1.98	1.12
12H-1, 135–140	Rh	36.38	1.38	—	—	—	—	—	—
13H-1, 121–126	Rh	39.54	2.23	0.60	0.24	0.10	0.01	1.79	1.00
14H-1, 135–140	Rh	41.38	1.28	0.53	0.28	0.11	0.01	2.09	1.81
15H-1, 126–131	Rh	44.59	1.44	0.59	0.24	0.09	0.01	2.06	2.09
347-M0065B-									
2H-1, 135–140	Rh	4.38	14.85	0.97	0.03	0.12	0.03	1.77	1.58
2H-2, 135–140	Rh	5.88	14.86	0.93	0.04	0.11	0.02	1.78	1.56
3H-1, 135–140	Rh	7.68	14.33	0.94	0.04	0.11	0.02	1.81	1.43
3H-2, 135–140	Rh	9.18	13.59	0.92	0.05	0.11	0.02	1.81	1.25
4H-1, 135–140	Rh	10.98	12.85	1.04	0.07	0.12	0.02	1.79	1.15
4H-2, 135–140	Rh	12.48	12.50	1.04	0.08	0.11	0.02	1.81	1.00
5H-1, 135–140	Rh	14.28	11.49	0.98	0.10	0.11	0.01	1.80	0.74
5H-2, 135–140	Rh	15.78	10.66	1.04	0.13	0.11	0.01	1.79	0.57
6H-1, 135–140	Rh	17.58	8.95	0.95	0.16	0.10	0.01	1.81	0.39
6H-2, 135–140	Rh	19.08	7.94	0.92	0.19	0.10	0.01	1.83	0.35
7H-1, 135–140	Rh	20.88	6.78	0.70	0.20	0.09	0.00	1.80	0.31
8H-1, 135–140	Rh	24.18	4.85	0.52	0.22	0.08	0.00	1.87	0.39
9H-1, 135–140	Rh	27.48	3.34	0.41	0.27	0.10	0.00	1.78	0.48
10H-1, 145–150	Rh	30.88	2.30	0.38	0.32	0.12	0.01	1.93	0.78
11H-1, 135–140	Rh	34.08	1.50	0.25	0.35	0.13	0.01	2.03	1.19
12H-1, 135–140	Rh	37.38	1.20	0.26	0.35	0.13	0.01	2.11	1.50
13H-1, 135–140	Rh	40.68	1.20	0.39	0.30	0.12	0.01	2.15	1.75
14H-1, 135–140	Rh	43.98	1.39	0.58	0.24	0.09	0.01	2.08	1.95
15H-1, 59–64	Rh	46.52	2.03	0.74	0.19	0.08	0.01	1.90	1.60
347-M0065C-									
2H-1, 130–140	Sq	3.35	15.84	0.91	0.03	0.11	0.03	1.72	1.48
2H-2, 130–130	Sq	4.80	15.21	0.87	0.03	0.11	0.03	1.74	1.35
3H-1, 135–145	Sq	6.70	15.29	0.86	0.04	0.11	0.02	1.77	1.45
3H-2, 115–115	Sq	7.95	14.64	0.89	0.04	0.10	0.02	1.77	1.24
4H-1, 130–140	Sq	9.95	13.86	0.84	0.05	0.09	0.02	1.76	1.03
4H-2, 135–135	Sq	11.45	12.15	0.94	0.07	0.10	0.02	1.76	0.93
5H-1, 135–145	Sq	13.30	13.19	0.97	0.08	0.10	0.02	1.77	0.72
5H-2, 140–140	Sq	14.80	11.08	0.88	0.09	0.09	0.01	1.76	0.53
6H-1, 135–145	Sq	16.60	10.07	0.80	0.12	0.08	0.01	1.77	0.36
6H-2, 140–140	Sq	18.10	8.76	0.86	0.15	0.08	0.01	1.91	0.32
7H-1, 130–140	Sq	19.85	7.80	0.70	0.15	0.08	0.00	1.79	0.29
7H-2, 140–140	Sq	21.40	6.65	0.62	0.17	0.07	0.00	1.81	0.30
8H-2, 35–45	Sq	23.70	5.49	0.55	0.21	0.08	0.00	1.83	0.40
9H-2, 70–80	Sq	27.35	3.69	0.46	0.27	0.10	0.00	1.81	0.57
10H-2, 105–115	Sq	31.00	1.72	0.47	0.44	0.17	0.01	1.99	1.26
11H-2, 45–55	Sq	33.70	2.35	0.23	0.27	0.11	0.01	1.91	1.00
12H-2, 65–75	Sq	37.20	1.26	0.29	0.34	0.15	0.01	2.07	1.82
13H-1, 135–140	Sq	39.68	1.52	0.48	0.26	0.11	0.01	1.93	1.40
14H-1, 135–140	Sq	42.98	1.40	0.58	0.25	0.10	0.01	2.01	1.77
15H-1, 135–140	Sq	46.28	1.67	0.66	0.21	0.08	0.01	1.99	2.01

Table T7 (continued).

Core, section, interval (cm)	Type	Depth (mbsf)	Cl^- based salinity	Na/Cl (mM/mM)	Ca/Cl (mM/mM)	Mg/Cl (mM/mM)	K/Cl (mM/mM)	Br/Cl (µM/mM)	B/Cl (µM/mM)
347-M0065C-									
2H-1, 54–59	Rh	2.57	15.52	0.87	0.03	0.10	0.02	1.67	1.25
3H-1, 67–72	Rh	6.00	14.84	0.87	0.03	0.11	0.02	1.76	1.34
3H-2, 47–52	Rh	7.30	14.65	0.90	0.04	0.11	0.02	1.77	1.24
4H-1, 56–61	Rh	9.19	12.84	0.90	0.05	0.10	0.02	1.76	1.10
5H-1, 90–95	Rh	12.83	12.36	0.90	0.07	0.09	0.01	1.75	0.71
5H-2, 88–93	Rh	14.31	11.49	0.83	0.08	0.08	0.01	1.76	0.49
6H-1, 112–117	Rh	16.35	10.01	0.90	0.11	0.08	0.01	1.75	0.34
6H-2, 112–117	Rh	17.85	8.96	0.91	0.16	0.09	0.01	1.78	0.33
7H-1, 104–109	Rh	19.57	7.88	0.83	0.17	0.08	0.00	1.77	0.27
8H-1, 135–140	Rh	23.18	5.58	0.65	0.23	0.09	0.00	1.82	0.35
9H-1, 134–139	Rh	26.47	4.00	—	—	—	—	—	—
10H-1, 92–97	Rh	29.35	2.78	0.39	0.30	0.11	0.01	1.86	0.61
11H-1, 134–139	Rh	33.07	—	—	—	—	—	—	—
12H-1, 65–70	Rh	35.68	1.26	—	—	—	—	—	—

Rh = Rhizon sample, Sq = squeezed sample. — = no data are reported for samples with insufficient pore water volumes.

Table T8. Concentration of methane in interstitial water, Site M0065.

Core, section, interval (cm)	Depth (mbsf)	CH_4 (mM)
347-M0065A-		
2H-1, 145–150	3.48	10.1
2H-2, 125–130	4.78	7.3
3H-1, 145–150	6.78	8.4
3H-2, 125–130	8.08	8.9
4H-1, 145–150	10.08	9.2
4H-2, 125–130	11.38	9.3
5H-1, 145–150	13.38	4.7
5H-2, 134–139	14.77	6.6
6H-1, 144–149	16.67	0.8
6H-2, 125–130	17.97	8.0
7H-1, 145–150	19.98	5.7
7H-2, 145–150	21.48	5.4
8H-1, 145–150	23.28	4.5
9H-1, 145–150	26.58	2.2
10H-1, 145–150	29.88	1.4
11H-1, 145–150	33.18	0.8
12H-1, 145–150	36.48	0.4
14H-1, 145–150	41.48	0.3
15H-1, 136–141	44.69	0.3

Table T9. Total carbon (TC), total organic carbon (TOC), total inorganic carbon (TIC), and total sulfur (TS) in sediment, Site M0065.

Core, section, interval (cm)	Depth (mbsf)	TC (wt%)	TOC (wt%)	TIC (wt%)	TS (wt%)
347-M0065A-					
2H-1, 86–87	2.86	4.16	3.67	0.49	1.30
3H-2, 84–85	7.64	4.01	3.38	0.63	1.16
4H-3, 20–21	11.60	0.97	0.88	0.10	—
5H-1, 33–34	12.23	0.83	0.72	0.11	0.33
5H-2, 130–131	14.69	0.84	0.27	0.57	0.11
6H-2, 52–53	17.21	1.73	0.49	1.24	0.12
7H-2, 63–64	20.63	2.51	0.71	1.81	0.16
8H-1, 117–118	22.97	1.71	0.48	1.22	0.13
9H-2, 66.5–67.5	27.27	2.36	0.50	1.85	0.15
10H-2, 42–44	30.32	2.48	0.48	1.99	0.17
11H-1, 117–118	32.87	1.68	0.46	1.22	0.11
12H-2, 91–92	37.41	2.32	0.40	1.91	0.12
13H-1, 85–86	39.15	2.26	0.32	1.95	0.16
14H-1, 49–50	40.49	2.50	0.07	2.43	0.26
15H-1, 47–48	43.77	3.71	0.33	3.38	0.44
347-M0065B-					
2H-1, 74–75	3.74	4.44	3.99	0.45	1.53
3H-1, 100–101.5	7.30	3.97	3.38	0.59	1.23
4H-1, 70–71	10.30	2.16	1.93	0.23	—
5H-1, 33–34	13.23	1.04	0.41	0.64	—
5H-2, 33–34	14.73	0.42	0.38	0.05	—
6H-1, 79–80	16.99	2.05	0.50	1.55	0.12
7H-1, 50–51	20.00	1.23	0.51	0.71	0.10
8H-1, 50–51	23.30	3.06	0.91	2.15	0.22
9H-1, 50–51	26.60	1.80	0.51	1.29	0.10
10H-1, 50–51	29.90	2.34	0.53	1.81	0.12
11H-1, 50–51	33.20	1.98	0.47	1.51	0.12
12H-2, 82–83	38.32	2.33	0.40	1.93	0.12
13H-2, 44–45	41.24	2.29	0.05	2.24	0.20
14H-1, 130–131	43.90	3.34	0.23	3.11	0.27
15H-1, 37–38	46.27	3.39	0.70	2.68	0.71
347-M0065C-					
3H-1, 30–31	5.60	4.54	4.12	0.43	1.49
4H-1, 38–39	8.98	3.28	2.83	0.45	1.77
5H-1, 28–29	12.18	0.67	0.58	0.09	0.14
5H-2, 97–98	14.37	0.90	0.28	0.63	0.10
6H-1, 110–111	16.30	1.52	0.49	1.04	0.13
7H-1, 100–101	19.50	1.36	0.48	0.88	0.11
8H-1, 100–101	22.80	2.11	0.58	1.53	0.13
9H-1, 100–101	26.10	2.09	0.47	1.62	0.12
10H-1, 69–70	29.09	2.42	0.51	1.91	0.14
11H-1, 50–51	32.20	1.76	0.44	1.32	0.11
12H-1, 50–51	35.50	2.46	2.02	0.44	0.56
12H-2, 50–51	37.00	2.39	0.65	1.73	0.19
13H-1, 60–61	38.90	2.90	0.28	2.62	0.23
14H-2, 31–32	43.41	3.25	0.22	3.03	0.26
15H-1, 29–30	45.19	3.40	0.23	3.17	0.34

Table T10. Samples taken for cell counts by flow cytometry and acridine orange direct count (AODC), Hole M0059C.

Core, section	Depth (mbsf)	Cytometer counts (log cells/cm^3)	AODC (log cells/cm^3)
347-M0065C-			
2H-2, 3	3.53	8.97	10.09
2H-2, 146			9.81
3H-2, 3	6.83	8.75	10.05
3H-2, 126	8.06		9.37
4H-2, 3	10.13	8.21	9.29
4H-2, 136	11.46		8.38
5H-2, 3	13.43	8.06	7.79
5H-2, 136	14.76		8.29
6H-2, 3	16.73	8.62	8.37
7H-2, 3	20.03	7.92	7.98
8H-2, 3	23.33	7.85	8.26
9H-2, 3	26.63	8.03	8.14
10H-2, 3	29.93	8.61	8.18
11H-2, 3	33.23	8.26	8.16
12H-2, 3	36.53	8.50	8.25

Respective count data are presented in the last two columns in logarithmic format.

Table T11. Drilling fluid contamination, Hole M0065C.

Core	Depth (mbsf)	PFC (g/L)	LF fraction in sample	Contaminant (cells/cm^3)
347-M0065C-				
Core interior				
2H	3.45	3.67E–08	6.49E–03	1.73E+04
3H	6.75	4.95E–09	1.62E–06	4.32E+00
4H	10.05	2.95E–08	5.05E–05	1.35E+02
5H	13.35	2.41E–08	3.19E–04	8.51E+02
6H	16.65	BD	NA	NA
7H	19.95	BD	NA	NA
8H	23.25	1.75E–09	5.41E–05	1.45E+02
9H	26.55	8.53E–10	6.01E–06	1.60E+01
10H	29.85	2.96E–10	8.59E–06	2.29E+01
11H	33.15	2.14E–09	8.08E–05	2.16E+02
12H	36.45	9.22E–10	4.65E–06	1.24E+01
Core halfway				
2H	3.45	2.91E–08	5.15E–03	1.38E+04
3H	6.75	3.29E–09	1.07E–06	2.87E+00
4H	10.05	6.94E–09	1.19E–05	3.17E+01
5H	13.35	2.22E–09	2.94E–05	7.84E+01
6H	16.65	3.07E–09	5.23E–05	1.40E+02
7H	19.95	7.43E–08	4.45E–04	1.19E+03
8H	23.25	1.14E–09	3.53E–05	9.42E+01
9H	26.55	2.12E–09	1.49E–05	3.99E+01
10H	29.85	4.09E–06	1.19E–01	3.17E+05
11H	33.15	2.24E–09	8.46E–05	2.26E+02
12H	36.45	4.85E–06	2.45E–02	6.54E+04
Core exterior				
2H	3.45	1.28E–07	2.26E–02	6.05E+04
3H	6.75	2.09E–09	6.82E–07	1.82E+00
4H	10.05	7.96E–09	1.36E–05	3.63E+01
5H	13.35	1.31E–09	1.73E–05	4.63E+01
6H	16.65	4.34E–09	7.38E–05	1.97E+02
7H	19.95	1.29E–09	7.70E–06	2.06E+01
8H	23.25	2.07E–10	6.41E–06	1.71E+01
9H	26.55	1.99E–07	1.40E–03	3.74E+03
10H	29.85	1.55E–08	4.49E–04	1.20E+03
11H	33.15	4.31E–09	1.63E–04	4.34E+02
12H	36.45	4.81E–09	2.43E–05	6.48E+01
Liner fluid				
2H	3.45	5.65E–06	NA	NA
3H	6.75	3.06E–03	NA	NA
4H	10.05	5.85E–04	NA	NA
5H	13.35	7.56E–05	NA	NA
6H	16.65	5.88E–05	NA	NA
7H	19.95	1.67E–04	NA	NA
8H	23.25	3.23E–05	NA	NA
9H	26.55	1.42E–04	NA	NA
10H	29.85	3.45E–05	NA	NA
11H	33.15	2.65E–05	NA	NA
12H	36.45	1.98E–04	NA	NA
Drilling fluid				
3H	6.75	2.98E–07	NA	NA
3H	6.75	4.29E–05	NA	NA
9H	26.55	1.78E–05	NA	NA
9H	26.55	1.80E–05	NA	NA
9H	26.55	6.33E–07	NA	NA
13H	38.30	1.25E–06	NA	NA
13H	38.30	1.28E–06	NA	NA
15H	44.90	1.55E–04	NA	NA
15H	44.90	8.25E–05	NA	NA

Samples taken from interior, halfway or exterior positions in piston cores, in liner fluid and in drilling fluid. The contaminant cell numbers in samples represent an estimated potential maximum. PFC = perfluorocarbon tracer, LF = liner fluid. BD = below detection, NA = not applicable.

Table T12. Composite depth scale, Site M0065.

Core	Offset (m)	Top depth (mbsf)	Top depth (mcd)
347-M0065A-			
2H	0.00	2.0	2.00
3H	0.00	5.3	5.30
4H	0.47	8.6	9.07
5H	0.47	11.9	12.37
6H	0.47	15.2	15.67
7H	0.47	18.5	18.97
8H	0.47	21.8	22.27
9H	0.62	25.1	25.72
10H	0.62	28.4	29.02
11H	0.62	31.7	32.32
12H	0.62	35.0	35.62
13H	0.62	38.3	38.92
14H	1.89	40.0	41.89
15H	2.52	43.3	45.82
347-M0065B-			
2H	0.16	3.0	3.16
3H	0.22	6.3	6.52
4H	0.22	9.6	9.82
5H	–0.24	12.9	12.66
6H	–0.52	16.2	15.68
7H	–0.55	19.5	18.95
8H	–0.46	22.8	22.34
9H	–0.46	26.1	25.64
10H	–0.46	29.4	28.94
11H	–0.49	32.7	32.21
12H	0.47	36.0	36.47
13H	0.63	39.3	39.93
14H	0.44	42.6	43.04
15H	0.88	45.9	46.78
347-M0065C-			
2H	–0.16	2.0	1.84
3H	0.07	5.3	5.37
4H	0.47	8.6	9.07
5H	0.50	11.9	12.40
6H	0.60	15.2	15.80
7H	0.52	18.5	19.02
8H	0.61	21.8	22.41
9H	0.52	25.1	25.62
10H	0.62	28.4	29.02
11H	0.62	31.7	32.32
12H	0.35	35.0	35.35
13H	1.02	38.3	39.32
14H	1.02	41.6	42.62
15H	0.43	44.9	45.33

Table T13. Splice tie points, Site M0065.

Hole, core, section, interval (cm)	Depth (mbsf)	Depth (mcd)		Hole, core, section, interval (cm)
347-				347-
M0065A-2H-4, 22	5.40	5.40	Append	M0065A-3H-1, 10
M0065A-3H-4, 19	8.70	9.16	Append	M0065A-4H-1, 9
M0065A-4H-2, 100	11.35	11.57	Tie to	M0065B-4H-2, 24
M0065B-4H-3, 13	12.50	12.96	Tie to	M0065A-5H-1, 59
M0065A-5H-2, 102	15.13	14.89	Tie to	M0065B-5H-2, 72
M0065B-5H-4, 12	15.57	16.04	Tie to	M0065A-6H-1, 37
M0065A-6H-3, 43	18.60	19.07	Append	M0065A-7H-1, 10
M0065A-7H-4, 21	21.90	22.36	Append	M0065A-8H-1, 9
M0065A-8H-4, 30	25.18	25.80	Append	M0065A-9H-1, 8
M0065A-9H-4, 15	28.48	29.10	Append	M0065A-10H-1, 8
M0065A-10H-4, 13	31.78	32.40	Append	M0065A-11H-1, 8
M0065A-11H-4, 15	35.08	35.70	Append	M0065A-12H-1, 8
M0065A-12H-2, 28	36.93	37.40	Tie to	M0065B-12H-1, 93
M0065B-12H-2, 156	38.92	39.54	Tie to	M0065A-13H-1, 61
M0065A-13H-1, 141	39.31	40.34	Tie to	M0065C-13H-1, 101
M0065C-13H-2, 92	41.12	41.75	Tie to	M0065B-13H-2, 32
M0065B-13H-2, 136	40.90	42.80	Tie to	M0065A-14H-1, 90
M0065A-14H-2, 64	43.60	44.04	Tie to	M0065B-14H-1, 99
M0065B-14H-2, 134	45.45	45.88	Tie to	M0065C-15H-1, 54
M0065C-15H-2, 41	44.73	47.25	Tie to	M0065A-15H-1, 143

Table T14. Sound velocity data for lithostratigraphic units, Site M0065.

Unit	Thickness of unit (m)	Sound velocity (m/s)*	TWT (ms)	Depth (m)	Depth (mbsf)
Seafloor	87.0	1475	0.118	87.0	0.0
I	9.2	1409	0.131	96.2	9.2
II	4.0	1439	0.137	100.2	13.2
IIIa	22.8	1448	0.168	121.0	36.0
IIIb	0.7	1480	0.169	123.7	36.7
IV	9.9	1525	0.182	133.6	46.6

* = sound velocities are based on values measured during the OSP. TWT = two-way traveltime.